



HAL
open science

FFAT motif phosphorylation controls formation and lipid transfer function of inter-organelle contacts

Thomas Di Mattia, Arthur Martinet, Souade Ikhlef, Alastair G Mcewen, Yves Nominé, Corinne Wendling, Pierre Poussin-courmontagne, Laetitia Voilquin, Pascal Eberling, Frank Ruffenach, et al.

► To cite this version:

Thomas Di Mattia, Arthur Martinet, Souade Ikhlef, Alastair G Mcewen, Yves Nominé, et al.. FFAT motif phosphorylation controls formation and lipid transfer function of inter-organelle contacts. EMBO Journal, 2020, 39 (23), 10.15252/emj.2019104369 . hal-03045974

HAL Id: hal-03045974










<https://hal.science/hal-03045974v1>

Submitted on 8 Dec 2020

HAL is a multi-disciplinary open access archive for the deposit and dissemination of scientific research documents, whether they are published or not. The documents may come from teaching and research institutions in France or abroad, or from public or private research centers.

L'archive ouverte pluridisciplinaire **HAL**, est destinée au dépôt et à la diffusion de documents scientifiques de niveau recherche, publiés ou non, émanant des établissements d'enseignement et de recherche français ou étrangers, des laboratoires publics ou privés.

FFAT motif phosphorylation controls formation and lipid transfer function of inter-organelle contacts

Thomas Di Mattia^{1,2,3,4,†} , Arthur Martinet^{1,2,3,4,†} , Souade Ikhlef^{5,†}, Alastair G McEwen^{1,2,3,4} , Yves Nominé^{1,2,3,4} , Corinne Wendling^{1,2,3,4}, Pierre Poussin-Courmontagne^{1,2,3,4}, Laetitia Voilquin^{1,2,3,4} , Pascal Eberling^{1,2,3,4}, Frank Ruffenach^{1,2,3,4}, Jean Cavarelli^{1,2,3,4}, John Slee⁶, Timothy P Levine⁶ , Guillaume Drin⁵ , Catherine Tomasetto^{1,2,3,4,*}  & Fabien Alpy^{1,2,3,4,**} 

Abstract

Organelles are physically connected by membrane contact sites. The endoplasmic reticulum possesses three major receptors, VAP-A, VAP-B, and MOSPD2, which interact with proteins at the surface of other organelles to build contacts. VAP-A, VAP-B, and MOSPD2 contain an MSP domain, which binds a motif named FFAT (two phenylalanines in an acidic tract). In this study, we identified a non-conventional FFAT motif where a conserved acidic residue is replaced by a serine/threonine. We show that phosphorylation of this serine/threonine is critical for non-conventional FFAT motifs (named Phospho-FFAT) to be recognized by the MSP domain. Moreover, structural analyses of the MSP domain alone or in complex with conventional and Phospho-FFAT peptides revealed new mechanisms of interaction. Based on these new insights, we produced a novel prediction algorithm, which expands the repertoire of candidate proteins with a Phospho-FFAT that are able to form membrane contact sites. Using a prototypical tethering complex made by STARD3 and VAP, we showed that phosphorylation is instrumental for the formation of ER-endosome contacts, and their sterol transfer function. This study reveals that phosphorylation acts as a general switch for inter-organelle contacts.

Keywords cholesterol; inter-organelle contact; lipid transfer protein; regulation; small linear motif

Subject Categories Membrane & Trafficking; Organelles

DOI 10.15252/embj.2019104369 | Received 28 December 2019 | Revised 1 September 2020 | Accepted 7 September 2020

The EMBO Journal (2020) e104369

Introduction

The endoplasmic reticulum (ER) is a membrane-bound organelle primarily involved in protein and lipid synthesis. The ER consists of the nuclear envelope as well as tubes and sheets spreading throughout the cytosol up to the plasma membrane (PM) (Westrate *et al*, 2015). In the cytosol, the ER physically contacts other organelles including mitochondria, endosomes/lysosomes, autophagic structures, peroxisomes, lipid droplets, and the PM. These contacts, termed membrane contact sites (MCSs), correspond to close appositions, usually within 30 nm, of the ER membrane with the limiting membrane of another organelle; they do not result in the fusion of the two membranes (Levine & Loewen, 2006; Wu *et al*, 2018). MCSs are involved in major cellular processes such as lipid and calcium transport, and organelle positioning and dynamics (Wu *et al*, 2018; Prinz *et al*, 2019).

Contacts between the ER and another organelle require tether proteins that bridge their two membranes via protein–membrane or protein–protein interactions. The ER possesses three major receptors at its surface which allow the recruitment of proteins associated with the membrane of other organelles. These proteins named vesicle-associated membrane protein-associated proteins (VAP) A and B, and motile sperm domain-containing protein 2 (MOSPD2), are members of the Major Sperm protein (MSP) domain-containing family. VAP-A, VAP-B, and MOSPD2 are anchored in the ER membrane by a carboxyl-terminal transmembrane domain with their MSP domain projecting into the cytosol. The MSP domains of VAP-A/VAP-B/MOSPD2 interact with small linear motifs named FFAT [two phenylalanines (FF) in an acidic tract (AT)] (Loewen *et al*, 2003; Murphy & Levine, 2016; Di Mattia *et al*, 2018). Contact sites are built by the direct binding between VAP-A/VAP-B/MOSPD2 at the ER surface and FFAT-containing partners which are bound to another organelle (such as endosomes, mitochondria,

1 Institut de Génétique et de Biologie Moléculaire et Cellulaire (IGBMC), Illkirch, France

2 Institut National de la Santé et de la Recherche Médicale (INSERM), U 1258, Illkirch, France

3 Centre National de la Recherche Scientifique (CNRS), UMR 7104, Illkirch, France

4 Université de Strasbourg, Illkirch

5 Institut de Pharmacologie Moléculaire et Cellulaire, Université Côte d'Azur, CNRS, Valbonne, France

6 UCL Institute of Ophthalmology, London, UK

*Corresponding author. Tel: +33 3 88 65 34 24; Fax: +33 3 88 65 32 01; E-mail: Catherine-Laure.Tomasetto@igbmc.fr

**Corresponding author. Tel: +33 3 88 65 35 19; Fax: +33 3 88 65 32 01; E-mail: Fabien.Alpy@igbmc.fr

†These authors contributed equally to this work

peroxisomes, the Golgi) or the PM (Amarilio *et al*, 2005; Kawano *et al*, 2006; Rocha *et al*, 2009; De Vos *et al*, 2012; Alpy *et al*, 2013; Mesmin *et al*, 2013; Dong *et al*, 2016; Costello *et al*, 2017a, b; Di Mattia *et al*, 2018; Johnson *et al*, 2018; Kirmiz *et al*, 2018).

MCSs are functional structures that physically attach two distinct organelles to each other. Visualization of contacts by microscopy in live cells revealed that they are dynamic, with organelles associating and dissociating over time (Friedman *et al*, 2013; Valm *et al*, 2017). This observation implies that mechanisms regulating these processes must exist. While the molecular organization and function of MCSs are better understood, the regulation of the formation and disassembly of these structures remains mostly unknown. In this study, we discovered that some partners of VAP-A/VAP-B/MOSPD2 possess a special type of FFAT motif that can be phosphorylated on a discrete site, and that we consequently named Phospho-FFAT. The phosphorylation of Phospho-FFATs is essential for the interaction of VAP-A/VAP-B/MOSPD2 with their Phospho-FFAT-containing partners. This reveals the existence of a general molecular mechanism regulating inter-organelle contact formation and function.

Results

Identification and functional characterization of a novel category of FFAT motifs potentially regulated by phosphorylation

Conventional FFATs have seven core residues: E₁F₂F₃D₄A₅X₆E₇, and an acidic flanking region (Fig 1A) (Loewen *et al*, 2003; Murphy & Levine, 2016). The residue at the fourth position is invariably acidic, either E or D; its substitution by an alanine precludes the interaction with the MSP domain (Loewen *et al*, 2003; Kawano *et al*, 2006). A survey of the literature revealed that some FFAT sequences differ from the conventional sequence: Their core FFAT motif contains a serine or a threonine residue at the 4th position instead of an acidic residue (Fig 1A). Because serine and threonine are polar amino acids that can gain a negative charge once their hydroxyl group is phosphorylated, we surmised that these residues might be phosphorylated to be able to bind the MSP domain. We identified six distinct VAP-A/VAP-B/MOSPD2 partners with an FFAT motif having this characteristic: STARD3 (steroidogenic acute regulatory (StAR)-related lipid transfer domain-containing 3), a late endosome (LE) protein involved in ER-LE cholesterol transport; FIP200 (FAK family kinase-interacting protein of 200 kDa), also known as RB1-inducible coiled-coil protein 1 (RB1CC1; RBCC1), a cytosolic protein involved in autophagosome formation (Hara *et al*, 2008; Zhao *et al*, 2018); Mitoguardin2 (MIGA2), also known as FAM73B, a mitochondrial outer membrane protein involved in mitochondria dynamics (Huttlin *et al*, 2015; Murphy & Levine, 2016; Zhang *et al*, 2016; Freyre *et al*, 2019); PTPIP51 (protein tyrosine phosphatase-interacting protein-51, aka regulator of microtubule dynamics protein 3, RMDN3; RMD3), a mitochondria protein involved in ER-mitochondria contact formation and possessing two FFATs, a conventional one and a non-conventional FFAT with a threonine at the 4th position (Stoica *et al*, 2014; Murphy & Levine, 2016; Huttlin *et al*, 2017; Di Mattia *et al*, 2018); and Kv2.1 and Kv2.2 (also known as potassium voltage-gated channel subfamily B member 1 (KCNB1) and KCNB2, respectively) which are voltage-gated potassium channels involved in neuronal excitability and in the formation of ER-PM

contacts (Lim *et al*, 2000; Fox *et al*, 2015; Johnson *et al*, 2018; Kirmiz *et al*, 2018) (Fig 1A).

To test whether these non-conventional FFAT motifs are genuine binding sites, we examined the binding of the six proteins identified above to VAPs and MOSPD2. More precisely, we asked whether the phosphorylation of the 4th residue of their FFAT motifs was implicated in binding with the MSP domain. To this end, we carried out pull-down assays of whole cell protein extracts using synthetic biotinylated peptides encompassing STARD3, FIP200, MIGA2, PTPIP51, Kv2.1, and Kv2.2 FFAT sequences whose 4th residue (serine or threonine) was either phosphorylated or not (Fig 1B). These peptides, and a negative control peptide with a random sequence (Fig 1B), were attached to streptavidin beads, and incubated with HeLa cell protein extracts. Bound proteins were detected by SDS-PAGE followed by Western blot using antibodies against VAP-A, VAP-B, and MOSPD2 (Fig 1C). Peptides corresponding to the non-phosphorylated FFAT motifs of STARD3, FIP200, MIGA2, PTPIP51, Kv2.1, and Kv2.2 retained none of the three proteins (Fig 1C). In contrast, VAP proteins were efficiently pulled down by all the peptides whose FFAT motif was phosphorylated (STARD3, FIP200, MIGA2, PTPIP51, Kv2.1, and Kv2.2). MOSPD2 interacted with the phosphorylated FFAT of STARD3, FIP200, and MIGA2, showing that the interaction of MOSPD2 with these FFATs requires phosphorylation. However, MOSPD2 did not interact with the phosphorylated FFAT of PTPIP51, Kv2.1, and Kv2.2. This result was surprising but not unexpected because the candidate proteins were primarily described as VAP-A and B partners in the literature (Stoica *et al*, 2014; Murphy & Levine, 2016; Huttlin *et al*, 2017; Johnson *et al*, 2018; Kirmiz *et al*, 2018). This suggests that the landscape of MOSPD2 partners is different from that of VAP proteins.

We then asked whether a conventional FFAT motif could be converted into a phosphorylation-dependent FFAT by replacing the acidic residue at the 4th position by a serine. To test this, we used the FFAT of oxysterol-binding protein-related protein 1 (OSBPL1A aka ORP1) (Loewen *et al*, 2003). We replaced D₄₇₈ (position 4 of the FFAT sequence) by a serine and by a phosphorylated serine (Fig 1B). We then performed peptide pull-down experiments. The FFAT of ORP1 efficiently pulled down VAP-A, VAP-B and MOSPD2 from the whole cell protein extract, whereas the non-phosphorylated D₄₇₈S mutant peptide did not (Fig 1D). Consistent with the idea that phosphorylation of the serine at position 4 of non-conventional FFAT motifs is crucial for the binding, we found that the peptide with a phosphorylated serine was able to trap VAP-A, VAP-B and MOSPD2.

Jointly, these data suggest that the interaction between VAP-A/VAP-B/MOSPD2 and several binding partners is activated by phosphorylation. To differentiate FFAT motifs characterized by a serine or a threonine in position 4 and switched on by phosphorylation from conventional ones, we named them Phospho-FFATs.

In silico identification of Phospho-FFAT motifs in the human proteome

In order to identify the human proteins possessing a Phospho-FFAT, we used an *in silico* approach. We designed a position weight matrix strategy which has previously served to identify conventional FFATs in many proteins (Mikitova & Levine, 2012; Murphy & Levine, 2016; Slee & Levine, 2019). It allows the identification of motifs with variations around an ideal FFAT sequence. Proteins are ranked based

on their best FFAT score, with a score 0 for an ideal FFAT sequence, and higher scores (up to 18.5) for distant motifs. We specifically focused on motifs which can be phosphorylated at position 4 of the core FFAT by imposing the presence of a serine or a threonine at that position. Among the 20,373 human proteins which were analyzed, 2,079 had a Phospho-FFAT score below 3 (Table EV1). It is noteworthy that to be effective, a Phospho-FFAT sequence has to be in the cytosolic part of the protein to be accessible to the MSP

domain of VAP-A/VAP-B/MOSPD2, and is likely present in an unstructured part of the protein. Therefore, true Phospho-FFATs likely represent only a subset of this list.

Because a large number of VAP-A/VAP-B/MOSPD2 partners have been identified by high-throughput proteomics (Orchard et al, 2014; Oughtred et al, 2019), we took advantage of these resources to test the 427 potential partners listed in the Biogrid and IntAct databases. For this analysis, we also included the MOSPD2 partners

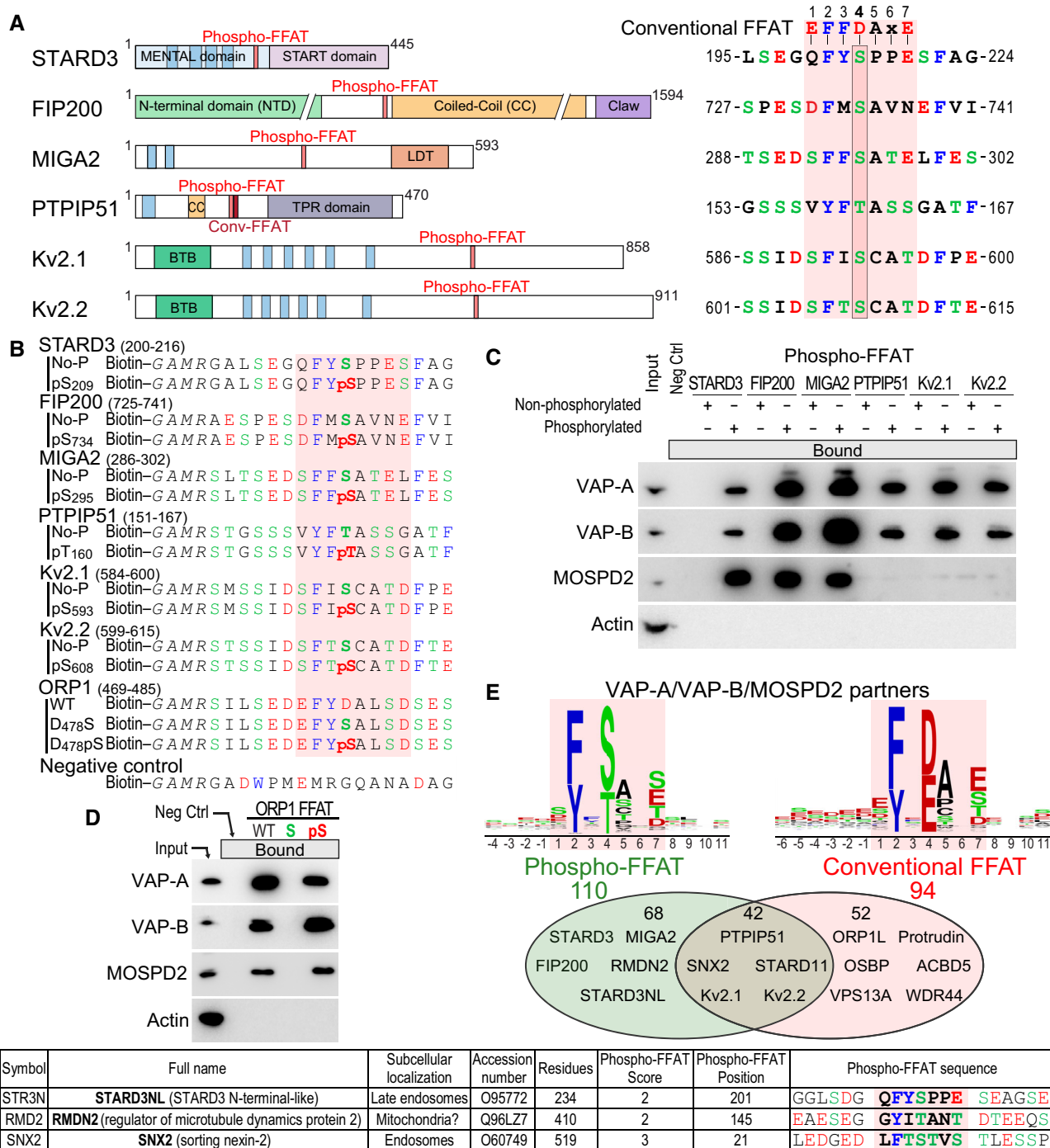


Figure 1.

Figure 1. Identification of novel category of FFAT motifs regulated by phosphorylation.

- A Schematic representation of STARD3, FIP200, MIGA2, PTPIP51, KCNB1 (Kv2.1), and KCNB2 (Kv2.2) proteins (left) and sequence of their Phospho-FFAT motif (7 core residues and 4 upstream and downstream residues) (right). Note that the 4th position of the FFAT (boxed) of these proteins is occupied by a serine or a threonine residue while conventional FFATs have an aspartic acid. Blue rectangles represent transmembrane helices. TPR: tetratricopeptide repeat; LDT: lipid droplet targeting domain; BTB: potassium channel tetramerization-type BTB domain.
- B Sequence of the peptides used for the pull-down assays. The peptides are composed of an amino-terminal biotin, a linker sequence and the FFAT sequence of STARD3 (residues 200–216), FIP200 (residues 725–741), MIGA2 (residues 286–302), PTPIP51 (residues 151–167), Kv2.1 (residues 584–600), Kv2.2 (residues 599–615), and ORP1 (residues 469–485) either without or with a phosphorylated residue (serine or threonine) at position 4 of the core FFAT motif. The negative control peptide is composed of a random sequence.
- C Western blot analysis of proteins pulled down using the peptides described in (B). The input fraction corresponds to HeLa cell total protein extract. Bound proteins were analyzed using anti-VAP-A, anti-VAP-B and anti-MOSPD2 antibodies. Actin was used as a loading control.
- D Western blot analysis of proteins pulled down using peptides comprising WT and mutant (D₄₇₈S and D₄₇₈P/S) ORP1 FFAT sequence peptides described in (B). Bound proteins were analyzed using anti-VAP-A, anti-VAP-B, and anti-MOSPD2 antibodies. Actin was used as a loading control.
- E Venn diagram of VAPs and/or MOSPD2 partners with FFAT scores between 0 and 3. Proteins with a Phospho-FFAT and a conventional FFAT are shown in green and red, respectively. A total of 42 proteins possesses both a Phospho and a conventional FFAT. Consensus sequences of the 110 Phospho-FFAT (left) and 94 conventional FFAT motifs (right) identified are shown as sequence logos.
- F List of selected VAP-A, VAP-B, or MOSPD2 partners having a potential Phospho-FFAT motif. For a full list, see Table EV2.

Data information: Acidic (D and E) or phosphorylated residues (pS and pT), alcoholic (S and T), and aromatic (F and Y) residues are in red, green, and blue, respectively; the other residues are in black.

Source data are available online for this figure.

identified by ourselves using a proteomic approach (Di Mattia *et al.*, 2018). We screened the 488 known VAP-A/VAP-B/MOSPD2 partners for the presence of a candidate Phospho-FFAT motif. We identified 110 VAP-A/VAP-B/MOSPD2 partners with a significant Phospho-FFAT score (Table EV2). As expected, STARD3, FIP200, MIGA2, PTPIP51, Kv2.1, and Kv2.2 were attributed high scores by the algorithm, ranging from 0 to 2.5. Using another version of the algorithm allowing the identification of conventional FFATs, the two algorithms being mutually exclusive, 94 proteins were identified (Fig 1E). Interestingly, some proteins had two FFAT motifs, a conventional one and a Phospho-FFAT (Table EV2). This analysis suggests that Phospho-FFATs and conventional ones are equally distributed in the human proteome.

To further exploit this *in silico* approach, we sought for the presence of novel proteins containing a Phospho-FFAT motif which were not identified by the original FFAT-prediction algorithm (Mikitova & Levine, 2012; Murphy & Levine, 2016; Slee & Levine, 2019). We chose to describe three proteins of the list of 110 VAP-A/VAP-B/MOSPD2 partners (Table EV2) that are already characterized as being involved or potentially involved in the formation of MCSs (Fig 1F). One of these proteins is STARD3NL: The algorithm identified a Phospho-FFAT motif that is consistent with the current knowledge about this protein. STARD3NL is a LE protein homologous to STARD3 (Alpy *et al.*, 2002), involved in the formation of ER-endosome contacts by interacting with VAP-A/VAP-B/MOSPD2 (Alpy *et al.*, 2013; Di Mattia *et al.*, 2018). The FFAT of STARD3NL is highly similar to that of STARD3, with all the characteristics of a Phospho-FFAT, and therefore most likely requires phosphorylation to be active. Another example is RMDN2: This poorly characterized protein is homologous to PTPIP51 (aka RMDN3) notably in the amino-terminal transmembrane region. Interestingly, this region is responsible for the addressing of PTPIP51 to mitochondria (Lv *et al.*, 2006). This suggests that RMDN2 is also a mitochondrial protein; supporting this idea, RMDN2 was shown to be associated with the outer mitochondrial membrane in a high-throughput proteomics study (Go *et al.*, 2019). The algorithm identified a unique potential Phospho-FFAT motif in RMDN2 which is conserved with PTPIP51. This suggests that RMDN2 could be involved in ER-mitochondria

contacts regulated by phosphorylation. The last example is SNX2: The algorithm identified a Phospho-FFAT motif in SNX2 (Fig 1F), a component of the retromer complex which is implicated in ER-endosome contacts (Bonifacino & Rojas, 2006; Dong *et al.*, 2016). Interestingly, Dong *et al.* (2016) made a mutation analysis which is consistent with the Phospho-FFAT motif identified here. Therefore, it is likely that SNX2's interaction with VAP is regulated by phosphorylation.

To conclude, we developed an algorithm allowing the identification of candidate Phospho-FFATs in an unbiased manner. By crossing the list with the repertoires of MSP domain binding partners, this algorithm revealed that Phospho-FFATs are as common as conventional FFAT motifs in the human proteome.

Phosphorylation of the Phospho-FFAT allows binding with VAP-A and VAP-B

We selected one Phospho-FFAT-containing protein to study in-depth its association mechanism. We chose STARD3, one of the 15 human START proteins, a family of lipid transfer proteins (LTP) involved in the intracellular transport of lipids. We selected STARD3 because we previously reported that STARD3 makes ER-endosome contact sites by interacting with the ER proteins VAP-A, VAP-B, and MOSPD2 (Alpy *et al.*, 2013; Di Mattia *et al.*, 2018). These ER-endosome contacts are active regions that allow STARD3-mediated ER to endosome cholesterol transport (Alpy & Tomasetto, 2005; Wilhelm *et al.*, 2017). The Phospho-FFAT of STARD3 contains a serine residue at the 4th position (position 209 of the protein, hereafter referred to as S₂₀₉; note that hereafter numberings of FFAT residues are labeled as subscript) (Figs 1A and 2A). To determine whether this particular residue is phosphorylated, we first interrogated the public database PhosphoSitePlus (Hornbeck *et al.*, 2015)—which records post-translational modifications in a comprehensive manner—for the presence of phosphorylation in STARD3. We found that a series of phosphorylations in human and mouse STARD3 was described in and around the FFAT motif, on S₂₀₉, and on S₂₁₃, S₂₁₇, and S₂₂₁ (Fig 2A). To confirm these observations, we sought for STARD3 phosphorylation in HeLa cells, given that STARD3 makes

ER-endosome contacts in these cells (Alpy *et al*, 2013). To this aim, we expressed the GST-tagged STARD3 protein in HeLa cells, then purified the protein by affinity chromatography, and analyzed its phosphorylation by mass spectrometry. Once purified, the GST-STARD3 protein was digested with trypsin and chymotrypsin, and subjected to ion trap liquid chromatography–tandem mass spectrometry (LC/MS/MS) analysis. Phosphorylation was detected on S₂₀₉, S₂₁₃, S₂₁₇, and S₂₂₁ residues (Figs 2A and EV1). Together, these data show that STARD3 is phosphorylated on several serine residues in the core of its FFAT motif and in its vicinity.

We then explored whether VAP-A and VAP-B directly associate with the phosphorylated FFAT motif of STARD3 by *in vitro* binding assays using recombinant proteins and synthetic biotinylated peptides corresponding to the FFAT motif of STARD3. We produced in *Escherichia coli* and purified the MSP domains of VAP-A and VAP-B (Fig 2B). The MSP domain of VAP-A, with a double K94D/M96D mutation (hereafter called KD/MD mutant), which is defective in binding the FFAT motif (Kaiser *et al*, 2005), was used as a negative control. These proteins were then incubated with streptavidin beads coupled with biotinylated peptides corresponding to either a control, or non-phosphorylated or phosphorylated STARD3

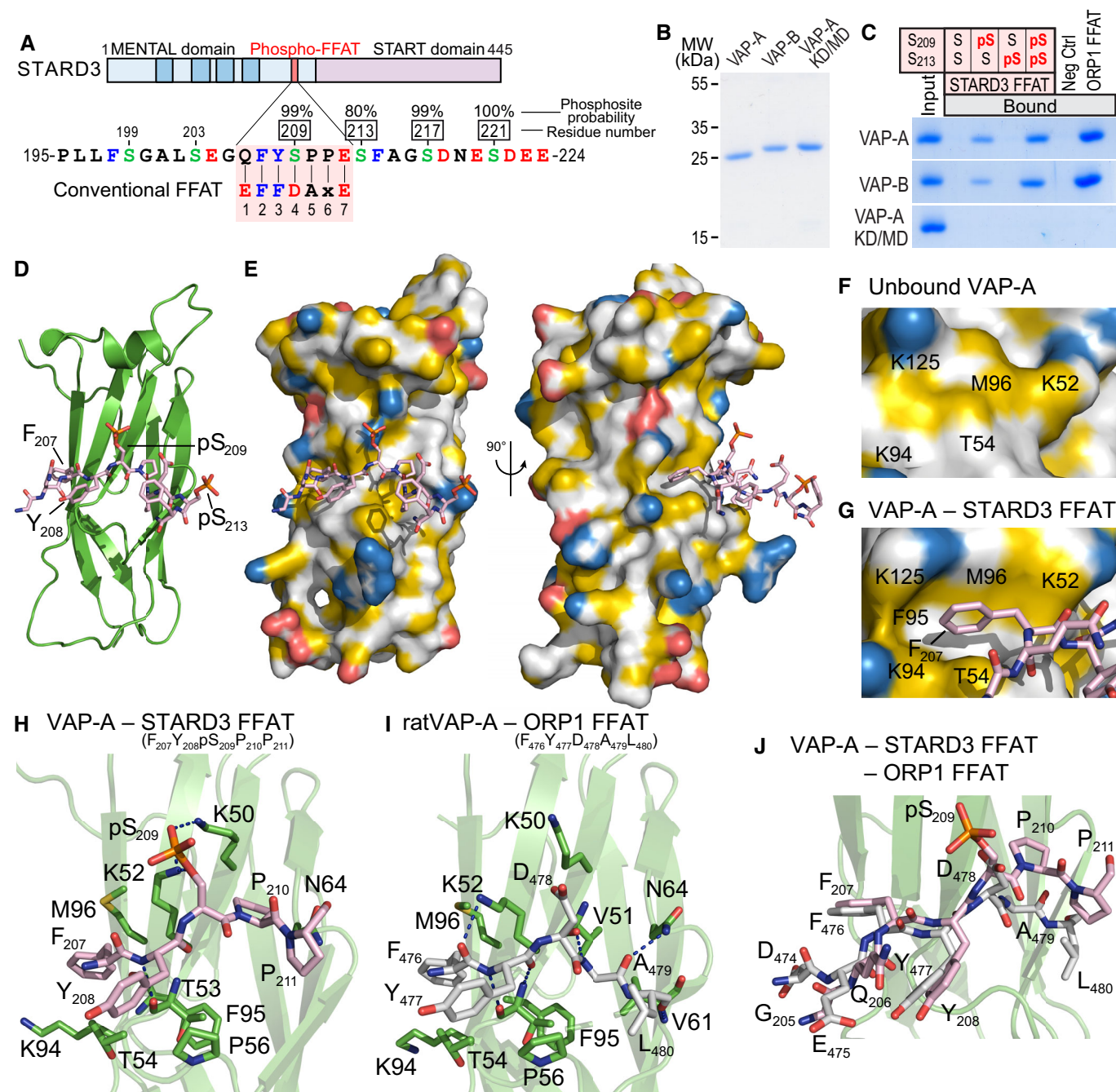


Figure 2.

Figure 2. STARD3 has a non-conventional FFAT motif which needs to be phosphorylated to form a complex with VAP proteins.

- A Schematic representation of STARD3. Transmembrane helices in the MENTAL domain are in dark blue. The Phospho-FFAT motif of STARD3 and the conventional FFAT motif sequences are aligned and highlighted in pink. Upper numbers correspond to the position of residues in STARD3. Lower numbers correspond to the position of residues in the FFAT sequence as described in (Loewen *et al*, 2003). Acidic (D and E), alcoholic (S and T), and aromatic (F and Y) residues are in red, green, and blue, respectively; the other residues are in black. Phosphorylated serines identified by LC/MS/MS are boxed, and the phosphosite probability determined with PhosphoRS is indicated.
- B Coomassie Blue staining of the recombinant wild-type MSP domains of VAP-A and VAP-B, and of the KD/MD mutant of VAP-A, after SDS-PAGE.
- C Recombinant MSP domains pulled down with peptides corresponding to the Phospho-FFAT motif of STARD3 (unphosphorylated; monophosphorylated on S₂₀₉ or S₂₁₃; bi-phosphorylated on S₂₀₉ and S₂₁₃), and with the control peptides were revealed by Coomassie Blue staining. The recombinant proteins subjected to the assay are shown in the input fraction.
- D, E Structure of the MSP domain of VAP-A in complex with a Phospho-FFAT motif. Ribbon diagram (D) and surface representation (E) of the MSP domain of VAP-A in complex with the Phospho-FFAT of STARD3 depicted in stick model. The protein surface is colored according to the YRB scheme, showing hydrophobic, negatively and positively charged atoms in yellow, red, and blue, respectively; the other atoms are in white (Hagemans *et al*, 2015).
- F, G Close-up view of the hydrophobic pocket region in the unbound (F) and the Phospho-FFAT-bound (G) VAP-A; residues of VAP-A constituting the pocket are indicated.
- H Close-up view of the structure near the Phospho-FFAT motif highlighting critical residues (in stick model) of human VAP-A present in the binding interface.
- I Close-up view of the structure near the conventional FFAT of ORP1 as described in (PDB ID: 1Z90; Kaiser *et al*, 2005), highlighting critical residues of rat VAP-A involved in the interaction. The nomenclature for rat VAP-A residues is based on the UniProt sequence (Q9Z270) and not on the PDB file 1Z90.
- J Superposition of the two structures shown in (H) and (I) showing the distinct conformations of the C-terminal parts of each peptide.

Data information: Phosphorous, nitrogen, oxygen, and sulfur atoms are colored in orange, blue, red, and yellow, respectively. Carbon atoms are shown in green and gray/pink in the MSP domain and the FFAT motif, respectively. The numbers of the peptide residues are noted in subscript.

FFAT motifs. We tested peptides bearing a phosphoserine either at position 209 or 213, or at both positions. We also included a peptide corresponding to the conventional FFAT motif of ORP1 (Loewen *et al*, 2003), and a random sequence of the same length, as positive and negative control, respectively (Fig EV3A). Retained proteins were eluted and analyzed by SDS-PAGE followed by Coomassie Blue staining (Fig 2C). The MSP domains of VAP-A and VAP-B interacted with the FFAT motif of ORP1, but did not interact with the non-phosphorylated STARD3 FFAT motif (Fig 2C). Only the peptides with a phosphorylation on serine 209 retained the MSP domain of VAP-A and VAP-B. Indeed, the peptide with a single phosphorylation on S₂₁₃ did not interact, while the ones with a phosphorylation on S₂₀₉ or two phosphorylations, on S₂₀₉ and S₂₁₃, interacted with the recombinant MSP domains.

Together, these experiments showed that phosphorylation of serine 209 is necessary and sufficient for the direct interaction of the STARD3 Phospho-FFAT with the MSP domains of VAP-A and VAP-B.

Structural insight into the interaction between VAP-A and a Phospho-FFAT

To gain structural insights about the interaction between the MSP domain and a Phospho-FFAT motif, we solved the crystal structure of the MSP domain of human VAP-A in complex with a peptide corresponding to the human phosphorylated STARD3 FFAT (residues 197–216) (PDB ID: 6TQR). The structure was resolved to 1.85 Å (from anisotropic data; 3 Å in the worst direction) by molecular replacement using the structure of rat VAP-A with ORP1 FFAT [PDB ID: 1Z90 (Kaiser *et al*, 2005)]. The asymmetric unit contains four copies of the MSP domain, two of which have the Phospho-FFAT bound. The structure of human VAP-A was strongly similar to that of rat VAP-A (rmsd of 0.538 Å over 119 C α s) (Fig 2D–J). Overall, the first residues of the core motif of the Phospho-FFAT bound the MSP domain similarly to the conventional FFAT motif of ORP1 (PDB ID: 1Z90; Kaiser *et al*, 2005). Indeed, F₂₀₇, the second residue of the FFAT motif, was bound to the hydrophobic pocket at the surface of

the MSP domain constituted by aliphatic parts of the side chains of K52, T54, K94, M96, and K125 of VAP-A (Fig 2G). The hydrogen bonds are also maintained between the main chain carbonyl and amide of Y₂₀₈ of the peptide and the main chain of T53 of VAP-A. The phosphorylated serine S₂₀₉ forms ionic bonds with two lysines of VAP-A, K50, and K52. Interestingly, the following core residue binds differently between the conventional and Phospho-FFAT: In the conventional FFAT motif of ORP1, the residue in position 5 is an alanine (Fig 2I). The side chain of A₄₇₉ sits in a hydrophobic pocket formed by V51, T53, V61, N64, and F95. Hydrogen bonds are also formed between the amide and carbonyl of A₄₇₉ with the carbonyl of V51, and the side chain amide of N64, respectively. This conformation of the peptide allows L₄₈₀, the 6th residue of the motif, to form a hydrogen bond between its carbonyl and the amide of V61, and a water-mediated contact between its amide and the carbonyls of P56 and Y59. However, in the Phospho-FFAT motif of STARD3, the residues in position 5 and 6 are both prolines (P₂₁₀ and P₂₁₁) (Fig 2H). This prevents P₂₁₀ from contacting the carbonyl of V51 of VAP-A. The side chain of P₂₁₀ no longer sits in the hydrophobic pocket, but instead makes hydrophobic contacts with the side chains of K50 and N64. This prevents any of the other contacts seen for residues 5 and 6 of the conventional FFAT motif. The difference in position of peptide also lifts the phosphoserine in position 4 closer to the side chain amides of K50 and K52, allowing it to make strong contacts.

The presence of two Phospho-FFAT-bound and two unbound chains in the asymmetric unit revealed conformation changes between the bound and unbound domains (Appendix Fig S1). We noted modifications involving the VAP residue F95 which is buried in the hydrophobic core of the domain, and M96 residue at its surface. These changes notably result in an opening of the hydrophobic pocket which allows F₂₀₇ of the Phospho-FFAT to bind (Fig 2F and G, and Appendix Fig S1).

Interestingly, depending of the nature of the negatively charged residue in position 4 of the FFAT (aspartate or phosphorylated serine, in a conventional and Phospho-FFAT motif, respectively), the interaction with the MSP domain of VAP-A is different. Indeed, superposition of the FFAT motifs of STARD3 and ORP1 showed that

the side chain of phosphorylated serine is longer than that of aspartate and forms an ionic bond with lysine K50 of VAP-A (Fig 2H–J). To determine whether this ionic bond contributes to the interaction *in vitro*, we produced the recombinant MSP domain of VAP-A in which K50 was replaced by a leucine (hereafter referred to as VAP-A K50L). Then, we tested the interaction of this VAP-A mutant with synthetic peptides corresponding to the phosphorylated FFAT of STARD3 or the conventional FFAT of ORP1 (Fig EV2A). Unlike wild-type VAP-A that interacted equally with the conventional and the Phospho-FFAT, VAP-A K50L only interacted with the conventional FFAT. Thus, the mutation of K50 in VAP-A impedes the interaction of its MSP domain with the Phospho-FFAT of STARD3, without affecting the ability of the protein to interact with the conventional FFAT of ORP1 *in vitro*. Given the high sequence identity (82%) between human VAP-A and VAP-B, we hypothesized that the interaction of FFAT motifs with each protein should be similar. Thus, we mutated the conserved lysine K43 in VAP-B and tested the interaction of the mutant protein with the conventional and the Phospho-FFAT *in vitro* (Fig EV2A). Similarly to VAP-A K50L, VAP-B K43L interacted with the conventional FFAT of ORP1, but not with the Phospho-FFAT of STARD3, while wild-type VAP-B interacted equally with the two types of FFAT motifs.

This structural analysis showed that the overall binding mode of a conventional FFAT and a Phospho-FFAT to VAP is different. While the first half of the core motif binds in an identical manner, it diverges in the other half with specific interactions being involved; more specifically, VAP-A K50 and VAP-B K43 residues are predominantly involved in binding the phosphorylated serine of the Phospho-FFAT.

***In vitro* biophysical characterization of VAPs interaction with Phospho-FFATs**

To determine in a quantitative manner the binding affinities between VAP-A and VAP-B, and a conventional FFAT or a Phospho-FFAT motif, we used the optical biosensing surface plasmon resonance (SPR) method. Either control, unphosphorylated or phosphorylated biotinylated peptides (Fig EV3A) were immobilized onto a sensor chip and several concentrations of recombinant MSP domains were injected. A strong association of every MSP domain with the conventional FFAT motif of ORP1 was measured, as indicated by the interaction profiles typical for a domain/peptide interaction (Fig EV3B). In contrast, no binding was seen with the non-phosphorylated FFAT of STARD3 (Fig 3A). Corroborating pull-down assays (Fig 2C), phosphorylation of S₂₀₉ in the peptide induced a dose-dependent signal increase (Fig 3B), thus confirming that a unique phosphorylation of this residue is critical for the interaction. The sensorgrams reached a steady-state response (R_{eq}) during the association phase which allowed the determination of affinities. The values of R_{eq} were fitted as a function of the MSP domain concentration assuming a Langmuir model. We have previously shown that the recombinant MSP domains of VAP-A and VAP-B form homodimers in solution (Di Mattia et al, 2018). Thus, the concentrations used to determine affinities correspond to those of VAP-A and VAP-B homodimers. Dissociation constants (K_D) of 5.6 ± 0.3 and 7.1 ± 0.3 μ M were determined by fitting the binding isotherms obtained for the interaction between the STARD3 FFAT pS₂₀₉ and the MSP domain of VAP-A and VAP-B, respectively (Fig 3B).

The presence of two phosphorylations on S₂₀₉ and S₂₁₃ slightly increased the affinity with the MSP domains (Fig 3D and E). To have a comprehensive understanding of the effect of phosphorylation near the FFAT motif, we also tested peptides containing a phosphoserine at position 203, even though it was not identified as being phosphorylated *in vivo*. The affinity with the MSP domain was further increased by the presence of three phosphorylations on S₂₀₃, S₂₀₉, and S₂₁₃ (Fig EV3D and E). Moreover, we found that STARD3 FFAT peptides phosphorylated on pS₂₁₃ only (Fig 3C) or pS₂₀₃ only (Fig EV3C) did not interact with any of the MSP domains. These data established the crucial role of phosphorylation on S₂₀₉ in the interaction process and showed that additional phosphorylation on residues in the vicinity of the core FFAT motif increased the affinity. The presence of several phosphorylated residues increases the number of negative charges in the FFAT peptide and increases interaction with the MSP domain. In agreement with the idea that electrostatic interactions play an important role, the interaction of the MSP domain of VAP-A and VAP-B with either a conventional FFAT or with a Phospho-FFAT was found to depend on the ionic strength of the buffer used (Fig EV3E).

These experiments showed that phosphorylation of serine at the 4th position in the core FFAT motif is critical for the direct interaction of the Phospho-FFAT with the MSP domains of VAP-A and VAP-B; in addition, the interaction occurs with a micromolar affinity, similar to that of a conventional FFAT motif.

Formation of the complex between STARD3 and VAPs requires phosphorylation of the Phospho-FFAT motif

Having established a key role of phosphorylation on serine at position 4 of the Phospho-FFAT of STARD3, the next step was to show that this phosphorylation was required for the assembly of the complex between STARD3 and VAP proteins.

First, we examined whether endogenous VAP-A and VAP-B could be isolated from whole cell protein extracts using synthetic biotinylated peptides corresponding to the FFAT motif of STARD3, either phosphorylated or not, as bait (Figs EV2C and EV3A). We tested peptides bearing a phosphoserine either at position 203, 209 or 213, or combinations of 2 or 3 phosphoserines at these positions. Each peptide was attached to streptavidin beads and incubated with HeLa cell protein extract. Bound proteins were eluted and analyzed by SDS–PAGE followed by Western blot using antibodies against VAP-A and VAP-B (Fig EV2C). As expected (Rocha et al, 2009; Di Mattia et al, 2018), the conventional ORP1 FFAT motif, used as positive control, efficiently pulled down VAP-A and VAP-B from the extract. Expected as well, the non-phosphorylated FFAT motif of STARD3 did not pull-down VAP-A or VAP-B (Fig EV2C). Consistent with the idea that phosphorylation at position 4 of the FFAT motif is crucial for the binding, we found that among the three monophosphorylated peptides, only the one with a phosphorylation on S₂₀₉ was able to trap VAP-A/VAP-B. Moreover, we found that among peptides bearing a combination of phosphorylations (2 or 3 phosphoserines) only the ones having phosphorylated S₂₀₉ efficiently pull-down VAP-A/VAP-B. In line with the SPR experiments, we noted that the presence of another phosphoserine in addition to pS₂₀₉ increased the interaction of the peptide with the VAP proteins, as indicated by the higher and lower amount of each protein in the bound and unbound fractions, respectively (Fig EV2C). These data confirmed the crucial role of the

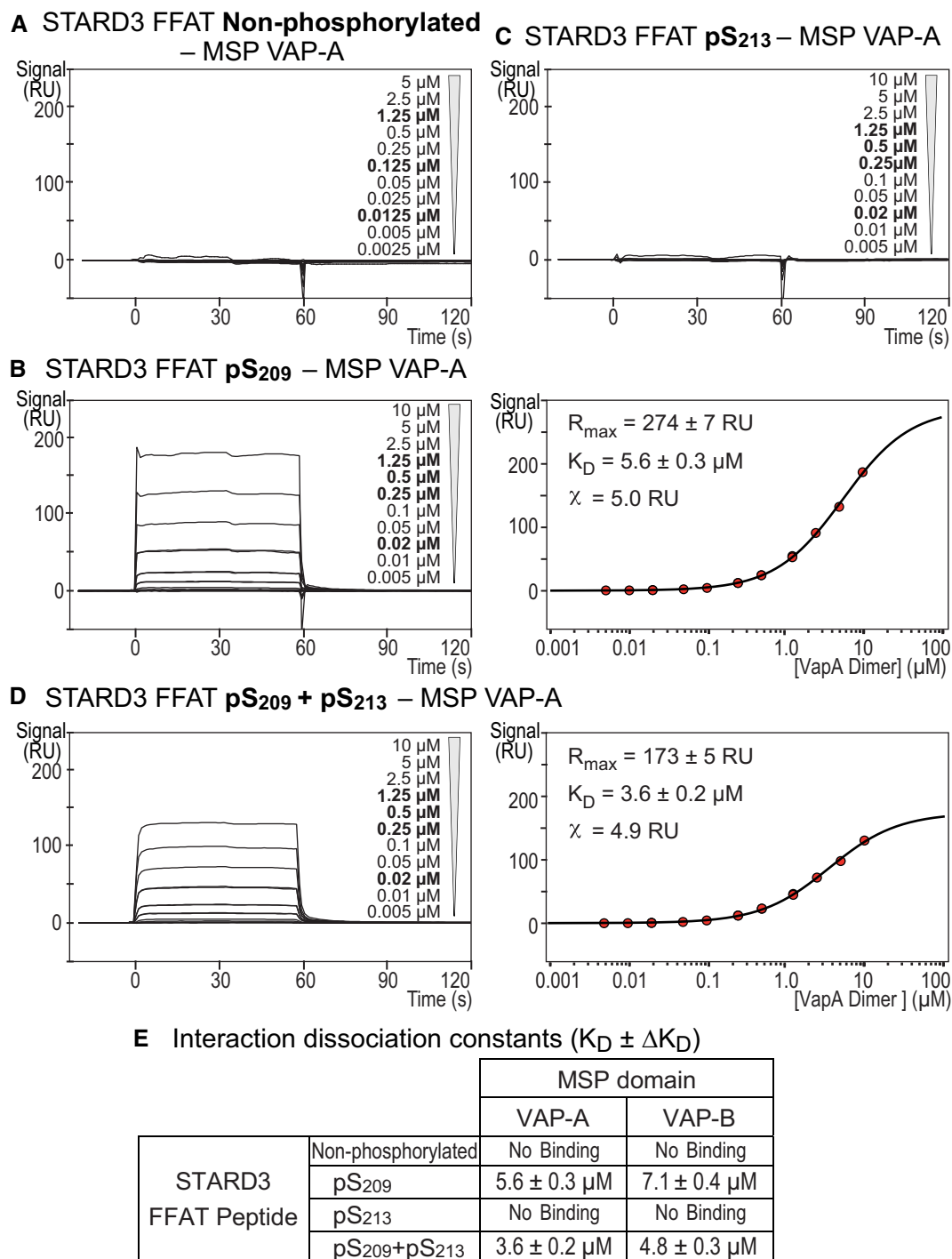


Figure 3. The MSP domain binds the phosphorylated Phospho-FFAT with an affinity in the micromolar range.

A–D Surface Plasmon Resonance analysis of the MSP domain of VAP-A binding onto immobilized unphosphorylated (A), monophosphorylated pS₂₀₉ (B) and pS₂₁₃ (C), and bi-phosphorylated pS₂₀₉ + pS₂₁₃ (D) STARD3 FFAT peptides. Representative sensorgrams resulting from the interaction between the MSP domain of VAP-A injected at different concentrations and the different FFAT peptides are shown in (A), (B left), (C), and (D left). Binding curves display the SPR signal (RU) as a function of time. Some samples were measured twice (concentrations printed in bold). Signal obtained for the negative control peptide immobilized on another flow cell is systematically subtracted, as well as the bulk effect recorded with buffer only. Steady-state analysis of the interaction between pS₂₀₉ (B right) and pS₂₀₉ + pS₂₁₃ (D right) STARD3 FFAT peptide, and the MSP domain of VAP-A. Equilibrium responses (R_{eq}) extracted from the left panel in association phase were plotted as a function of the dimeric MSP domain of VAP-A concentration, and fitted with a Langmuir binding model.

E Dissociation constants between peptides corresponding to different kind of FFAT motifs and the MSP domains of VAP-A and VAP-B. The kinetic experiments were performed at 25°C in 50 mM Tris-HCl pH 7.5, 75 mM NaCl buffer supplemented with 0.005% (*v/v*) surfactant polysorbate 20 (P20, GE Healthcare). Mean of *n* independent experiments: *n* = 2 for pS₂₀₉ and pS₂₀₉ + pS₂₁₃; 3 for pS₂₁₃; and 4 for the non-phosphorylated FFAT. Uncertainties are obtained from the standard deviation considering a *t*-distribution coefficient for a risk factor of 32%.

phosphorylation of S₂₀₉, corresponding to the 4th position of the core FFAT motif of STARD3, for the interaction of this motif with its ER-located VAP partners. Additional phosphorylations of S₂₀₃ and S₂₁₃ are not essential but strengthen the interaction.

We then analyzed the ability of full-length STARD3 to associate with VAP proteins. To test this, GFP-tagged VAP-A was co-expressed in HeLa cells with wild-type STARD3 or two mutants in which the S₂₀₉ was replaced either by a non-phosphorylatable residue, alanine (S₂₀₉A), or a phosphomimetic residue, aspartate (S₂₀₉D). The proteins were then immunoprecipitated using anti-GFP antibodies. The GFP-VAP-A KD/MD mutant was used as a negative control. As we previously showed (Alpy *et al*, 2013), wild-type STARD3 was co-immunoprecipitated with VAP-A (Fig 4A). In contrast, the STARD3 S₂₀₉A mutant was not co-precipitated (Fig 4A), suggesting that the interaction between VAP-A and STARD3 requires a phosphorylatable serine at position 4 of the FFAT motif. Replacing S₂₀₉ with the phosphomimetic aspartate residue did not, however, restore the VAP-A/STARD3 interaction. The tridimensional structure of VAP-A in complex with the Phospho-FFAT of STARD3 suggests that the proline residue in position 5 of the FFAT motif, by imposing a conformational rigidity in the peptide backbone, would prevent the aspartate residue from properly mimicking a phosphorylated serine, as it possesses a shorter side chain (Fig 2D–H). To circumvent this, we replaced this proline P₂₁₀ by an alanine, and serine S₂₀₉ by an aspartate, to generate the STARD3 S₂₀₉D/P₂₁₀A mutant. Remarkably, this mutant was co-immunoprecipitated with VAP-A (Fig 4A). The single mutant STARD3 P₂₁₀A showed an improved binding with VAP-A compared to WT STARD3 (Fig EV2D). In the context of the STARD3 Phospho-FFAT motif, the presence of the P₂₁₀ residue imposes a structural conformation enabling only the interaction with a phosphoserine at position 4. Thus, STARD3 requires a phosphorylatable serine in position 4 of its FFAT motif to interact with VAP-A; structural constraints explain that a single phosphomimetic mutation does not restore the interaction, only the double mutation restores binding. To substantiate this result, we repeated the experiments with VAP-B (Fig 4B). Like VAP-A, VAP-B bound to wild-type STARD3, but not with its non-phosphorylatable mutant STARD3 S₂₀₉A (Fig 4B). VAP-B, similarly to VAP-A, did not interact with STARD3 S₂₀₉D, while it interacted with STARD3 S₂₀₉D/P₂₁₀A. In agreement with these data, the recombinant MSP domain of VAP-A and VAP-B interacted with peptides corresponding to the STARD3 S₂₀₉D/P₂₁₀A mutant motif, while it did not interact with peptides having the STARD3 S₂₀₉D mutant motif (Fig EV2B).

Jointly, these results show that phosphorylation of the FFAT of STARD3 on its 4th position (S₂₀₉) is indispensable for the protein to interact with its partners VAP-A and VAP-B. Structural constraints explain that a single phosphomimetic mutation does not restore the interaction, only a double mutation S₂₀₉D/P₂₁₀A restores binding. Moreover, additional phosphorylations of serine outside the core motif are not required for the interaction, but when S₂₀₉ is phosphorylated, they increase the binding affinity.

Phosphorylation at the 4th residue of the Phospho-FFAT motif of STARD3 is necessary for ER-endosome contact formation *in vivo*

We previously reported that the creation of ER-endosome contacts, arising from the interaction between STARD3 and VAP-A or VAP-B, induces a striking relocalization of these latter two proteins from a

characteristic ER reticulated pattern to ER subdomains in contact with STARD3-positive endosomes (Alpy *et al*, 2013; Wilhelm *et al*, 2017). In contrast, when a mutant STARD3 with the FFAT core deleted was expressed, neither VAP-A or VAP-B were relocated toward ER sub-regions in contact with endosomes. Here, we performed similar experiments to address whether ER-endosome contact formation depends on STARD3 FFAT phosphorylation. We expressed VAP-A alone and in combination with either wild-type STARD3, its non-phosphorylatable counterpart S₂₀₉A mutant, or its phosphomimetic S₂₀₉D/P₂₁₀A mutant. When expressed alone, VAP-A was evenly present in the ER (Fig 4C). In the presence of wild-type STARD3, VAP-A was massively recruited toward endosomes (Fig 4D), with a positive correlation of VAP-A and STARD3 signals (Fig 4H). In contrast, in the presence of the S₂₀₉A mutant, VAP-A remained uniformly distributed in the ER (Fig 4E), with no signal correlation (Fig 4H). This phenotype was similar to what is observed in cells expressing VAP-A KD/MD or STARD3 F₂₀₇A/Y₂₀₈A (FFAT mutant named FA/YA) mutants, which are unable to form VAP/STARD3 complexes (Fig 4F and H; Alpy *et al*, 2013). Consistent with the biochemistry data, the phosphomimetic mutant STARD3 S₂₀₉D/P₂₁₀A induced the enrichment of VAP-A around endosomes (Fig 4G), and fluorescent signals were as correlated as the ones measured with wild-type STARD3 and VAP-A (Fig 4H). The colocalization of STARD3 (WT and mutants) with VAP-A was not affected by endogenous STARD3 protein (Fig EV4F). Jointly, these data showed that STARD3 phosphorylation on S₂₀₉ allows the formation of ER-endosome contacts *in vivo*.

Similar experiments were then performed with VAP-B (Fig EV4A–E). Akin to VAP-A, VAP-B was evenly distributed in the ER when expressed alone, and in the presence of the non-phosphorylatable STARD3 S₂₀₉A mutant, while it was recruited around endosomes by wild-type STARD3 and the phosphomimetic mutant STARD3 S₂₀₉D/P₂₁₀A (Fig EV4A–E).

Together, these data show that *in vivo* the phosphorylation of the STARD3 FFAT motif elicits the assembly of ER-endosome contacts made by a complex between STARD3 and either VAP-A or VAP-B.

Phosphorylation of the FFAT motif is essential for STARD3 sterol transfer function *in vitro*

Having established a novel mechanism of complex formation for a protein bearing a Phospho-FFAT motif like STARD3, we examined *in vitro* whether the phosphorylation of S₂₀₉ within the non-conventional FFAT motif was mandatory for STARD3 to be active, i.e., to connect the endosome and ER membranes, and to transfer sterol between them. To this end, we reconstituted the tethering complex *in vitro* with liposomes and recombinant proteins. First, we produced and purified recombinant proteins corresponding to the cytosolic part of STARD3 including the Phospho-FFAT motif, the START domain, and an N-terminal cysteine residue enabling the covalent attachment to liposomes doped with thiol-reactive MPB-PE lipid (Fig 5A). We produced this protein and a form constitutively phosphorylated on S₂₀₉, termed thereafter cSTD3 and pS₂₀₉ cSTD3, respectively. Because the production of recombinant proteins phosphorylated on a specific site is not possible using regular *E. coli*, we used a genomically recoded *E. coli* strain engineered to allow phosphoserine incorporation into recombinant proteins to produce pS₂₀₉ cSTD3 (Park *et al*, 2011; Pirman *et al*, 2015).

Recombinant proteins were analyzed by SDS-PAGE followed by SYPRO Orange staining. We observed one and two bands for cSTD3 and pS₂₀₉ cSTD3, respectively (Fig 5B). To have a tool able to detect STARD3 phosphorylation in the FFAT motif core, we developed a phospho-specific antibody recognizing STARD3 when

phosphorylated on S₂₀₉. (Appendix Fig S2). cSTD3 and pS₂₀₉ cSTD3 were detected by the anti-STARD3 antibody, but only the higher species in the pS₂₀₉ cSTD3 sample was additionally detected by the anti-phospho-STARD3-pS₂₀₉ antibody, thus showing that a fraction of protein is phosphorylated on S₂₀₉ (Fig 5B). As a confirmation, the

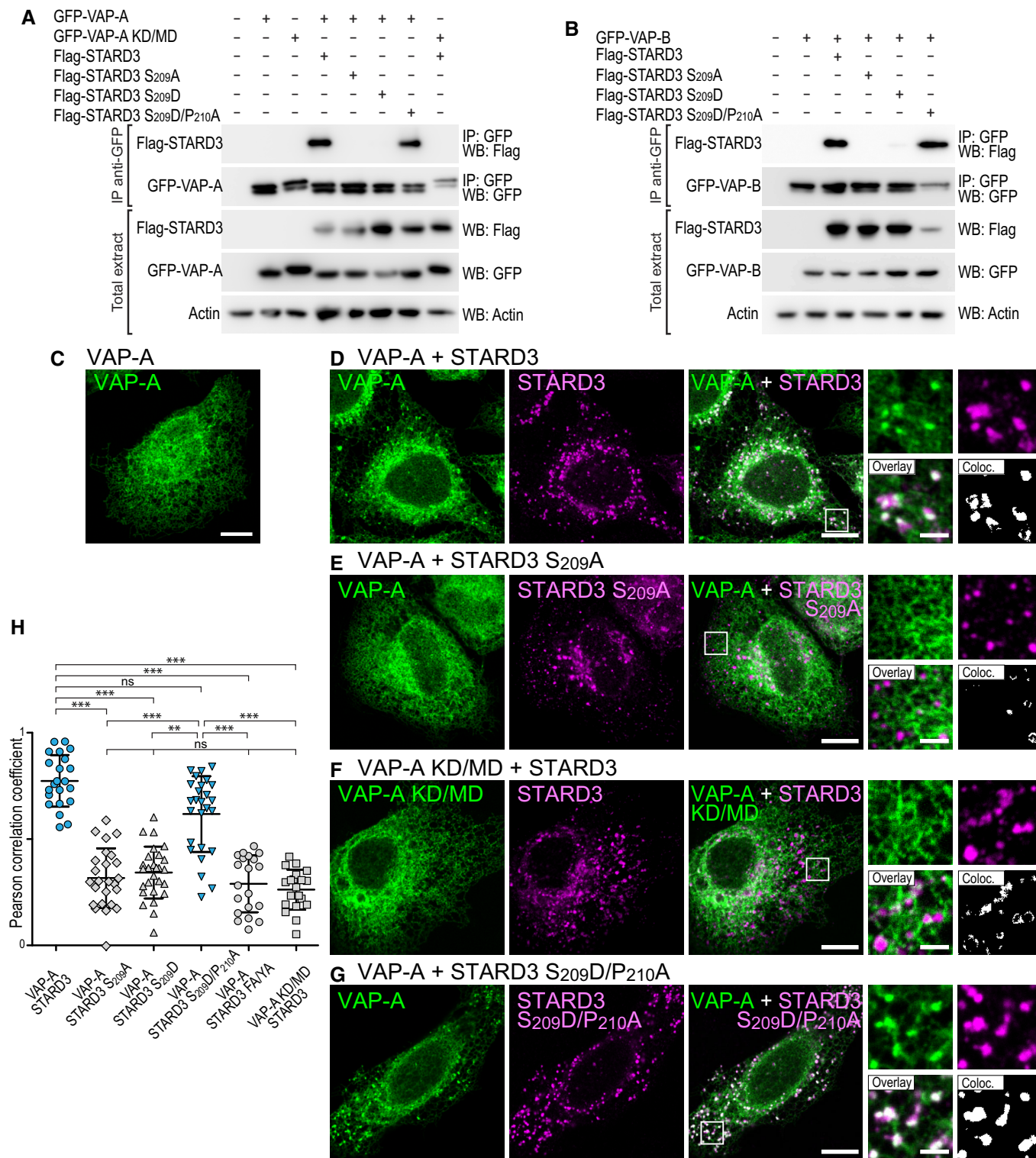


Figure 4.

Figure 4. *In vivo*, a unique phosphorylation of the Phospho-FFAT motif allows STARD3 and VAP-A/VAP-B complex formation and the establishment of ER-endosome contacts.

- A, B Binding assays. Immunoprecipitation (GFP-Trap) experiments between GFP-tagged VAP-A (WT and KD/MD mutant; A), VAP-B (B) and Flag-tagged STARD3 (WT and S₂₀₉A, S₂₀₉D, and S₂₀₉D/P₂₁₀A mutants). Please note that the mutations modify the FFAT and Phospho-FFAT scores of this region of STARD3: compared to WT STARD3 (Phospho-FFAT: 2.5; conventional FFAT: 6.5), the STARD3 S₂₀₉A mutant has both low Phospho-FFAT and FFAT scores (6.5), the S₂₀₉D mutant has a high conventional FFAT score (2.5) but a low Phospho-FFAT score (6.5), and the double mutant has a conventional FFAT score of 1.5 and a Phospho-FFAT score of 5.5. Approximately 5 μg of total protein extract was analyzed by Western blot using anti-Flag, anti-GFP, and anti-Actin antibodies. Immunoprecipitated material was analyzed using anti-Flag and anti-GFP antibodies.
- C–G Recruitment assays. GFP-VAP-A (C, D, E, G; green) and GFP-VAP-A KD/MD-expressing cells (F; green) were left untransfected (C) or transfected with Flag-STARD3 (D, F), Flag-STARD3 S₂₀₉A (E), and Flag-STARD3 S₂₀₉D/P₂₁₀A (G), and labeled using anti-Flag (magenta) antibodies. The subpanels on the right are higher magnification (3.5×) images of the area outlined in white. The Overlay panel shows merged green and magenta images. The Coloc panel displays a colocalization mask on which pixels where the green and the magenta channels co-localize are shown in white. Scale bars: 10 μm. Inset scale bars: 2 μm.
- H Pearson's correlation coefficients between VAP-A (WT or KD/MD mutant) and STARD3 (WT or S₂₀₉A, S₂₀₉D, S₂₀₉D/P₂₁₀A, FA/YA mutants) staining are shown. Each dot represents a single cell (number of cells: VAP-A–STARD3: 22; VAP-A–STARD3 S₂₀₉A: 25; VAP-A–STARD3 S₂₀₉D: 27; VAP-A–STARD3 S₂₀₉D/P₂₁₀A: 26; VAP-A–STARD3 FA/YA: 20; VAP-A KD/MD–STARD3: 20, from at least three independent experiments). Means and error bars (SD) are shown. Kruskal–Wallis with Dunn's multiple comparison test (**P < 0.01; ***P < 0.001).

Source data are available online for this figure.

analysis of pS₂₀₉ cSTD3 by mass spectrometry showed that it was present as two major species corresponding to the expected masses of the phosphorylated (MW = 28,366 Da) and non-phosphorylated (28,286 Da) proteins (Appendix Fig S3A). To confirm that the phosphorylation was indeed on S₂₀₉, recombinant pS₂₀₉ cSTD3 was digested with trypsin, and subjected to ion trap LC/MS/MS analysis (Appendix Fig S3B). This analysis confirmed that the phosphorylation site was on S₂₀₉. Thus, we produced and purified a pS₂₀₉ cSTD3 recombinant protein genuinely phosphorylated on S₂₀₉.

Next, to examine the tethering activity, cSTD3 or pS₂₀₉ cSTD3 proteins was attached to one population of liposomes called hereafter L_A liposomes. Liposome flotation assays confirmed that the two proteins were efficiently bound onto L_A liposomes (Appendix Fig S3C–E) and that liposome-bound pS₂₀₉ cSTD3 remained phosphorylated (Appendix Fig S3F). Then, we examined whether L_A liposomes bound with cSTD3 and pS₂₀₉ cSTD3 were able to physically associate with another population of liposomes (called L_B liposomes) covered with VAP-A by dynamic light scattering (Fig 5A and C). To prepare L_B liposomes, a recombinant VAP-A_{His6} protein with its carboxyl-terminal transmembrane region deleted was anchored to the surface of liposomes thanks to the presence of NTA-Ni²⁺ lipids (Wilhelm *et al*, 2017). When L_A liposomes covered by pS₂₀₉ cSTD3 were mixed with L_B liposomes bearing VAP-A, a rapid increase in the mean radius of liposomes (from ~ 90 nm up to 500 nm) occurred, indicating a connection between the two liposome populations (Fig 5C). This experiment was repeated with L_B liposomes lacking VAP-A, or covered with the VAP-A KD/MD mutant, and in both cases, no aggregation was seen (Fig 5C). For the cSTD3 protein, no aggregation was observed even in the presence of a functional VAP (Fig 5C). These results indicated that a unique phosphorylation of the S₂₀₉ serine in the Phospho-FFAT motif of STARD3 allows the protein to tether membranes in a VAP-dependent manner. It is noteworthy that the attachment of membranes does not provoke any fusion (Fig EV5) as measured by a standard FRET assay using an NBD-PE/Rhod-PE pair (Struck *et al*, 1981).

Once demonstrated that pS₂₀₉ cSTD3 protein allows for the tethering of two membranes, a further step was to study the kinetics of sterol transfer between them. To do so, we measured the intermembrane transfer of the fluorescent sterol dehydroergosterol (DHE) in real time by FRET (Fig 5D). L_B liposomes including both DHE

(10 mol%) and a second fluorescent lipid, dansyl-phosphatidylethanolamine (DNS-PE, 2.5 mol%), were covered with VAP-A_{His6} and added to L_A liposomes decorated with pS₂₀₉ cSTD3 (Fig 5A). The transport of DHE from L_B to L_A liposomes was followed by measuring the decrease in energy transfer from DHE to DNS-PE. A fast transport of DHE was observed within the first seconds, and DHE was entirely equilibrated between the two liposome populations after a few minutes. The initial DHE transport rate was 24.78 ± 1.07 DHE molecules/min per molecule of pS₂₀₉ cSTD3 (Fig 5E). In contrast, when L_B liposomes were covered by VAP-A KD/MD or were naked, the transport rates were four-time slower (7.10 ± 0.15 and 7.29 ± 1.04 DHE molecules/min per pS₂₀₉ cSTD3, respectively). When cSTD3 was unphosphorylated, the transport rates measured in the presence or absence of functional VAP were similar (6.87 and 10.45 DHE molecules/min per cSTD3, respectively).

Jointly, these results showed that using *in vitro* reconstitution assays, phosphorylation of the Phospho-FFAT motif of a liposome-bound STARD3 allows tethering with VAP-covered liposomes. The formation of this complex triggers a fast transfer of sterol between the two connected membranes. Thus, in a complete *in vitro* defined system, phosphorylation of STARD3's Phospho-FFAT drives membrane tethering by enabling STARD3/VAP complex formation that in turn allows the efficient transport of sterol mediated by the START domain.

Phosphorylation of the FFAT motif is essential for STARD3 sterol transfer function *in vivo*

To substantiate these data, we used the fluorescent probe filipin to follow cholesterol distribution in cells (Appendix Fig S4). As previously described (Wilhelm *et al*, 2017), compared to control cells, HeLa cells expressing STARD3 accumulated cholesterol in LEs that were labeled with the Lamp1 marker (Fig 6A, B, F, and G). Next, to directly assess the contribution of S₂₀₉ in the cholesterol accumulation phenotype, cholesterol was labeled in cells expressing the non-phosphorylatable STARD3 S₂₀₉A mutant. As expected from the fact that this mutant is unable to make ER-endosome contacts (Fig 4E), cholesterol did not accumulate in LEs of cells expressing STARD3 S₂₀₉A (Fig 6C and G). In contrast, the phosphomimetic mutation S₂₀₉D/P₂₁₀A restored cholesterol accumulation at a level comparable

to wild-type STARD3 (Fig 6D and G). To further assess the effect of a non-regulatable FFAT on STARD3, the STARD3 Conv-FFAT mutant was constructed by replacing the Phospho-FFAT of STARD3 by the conventional FFAT of the yeast transcriptional regulator Opi1p (EFFDASE) (Loewen *et al.*, 2003). Cells expressing the STARD3 Conv-FFAT mutant accumulated cholesterol in endosomes similarly to cells expressing the wild-type STARD3 (Fig 6E and G).

Together, these data show that the phosphorylation of S₂₀₉ is necessary for STARD3 function in cholesterol transport toward LEs. Of interest, replacement of a Phospho-FFAT with a phosphomimetic mutant or a conventional FFAT motif, transforming it into a constitutively active motif, restored the transport function of STARD3. These results support the idea that the regulation by phosphorylation of the Phospho-FFAT of STARD3 is a way to mitigate the effect of the protein on sterol distribution.

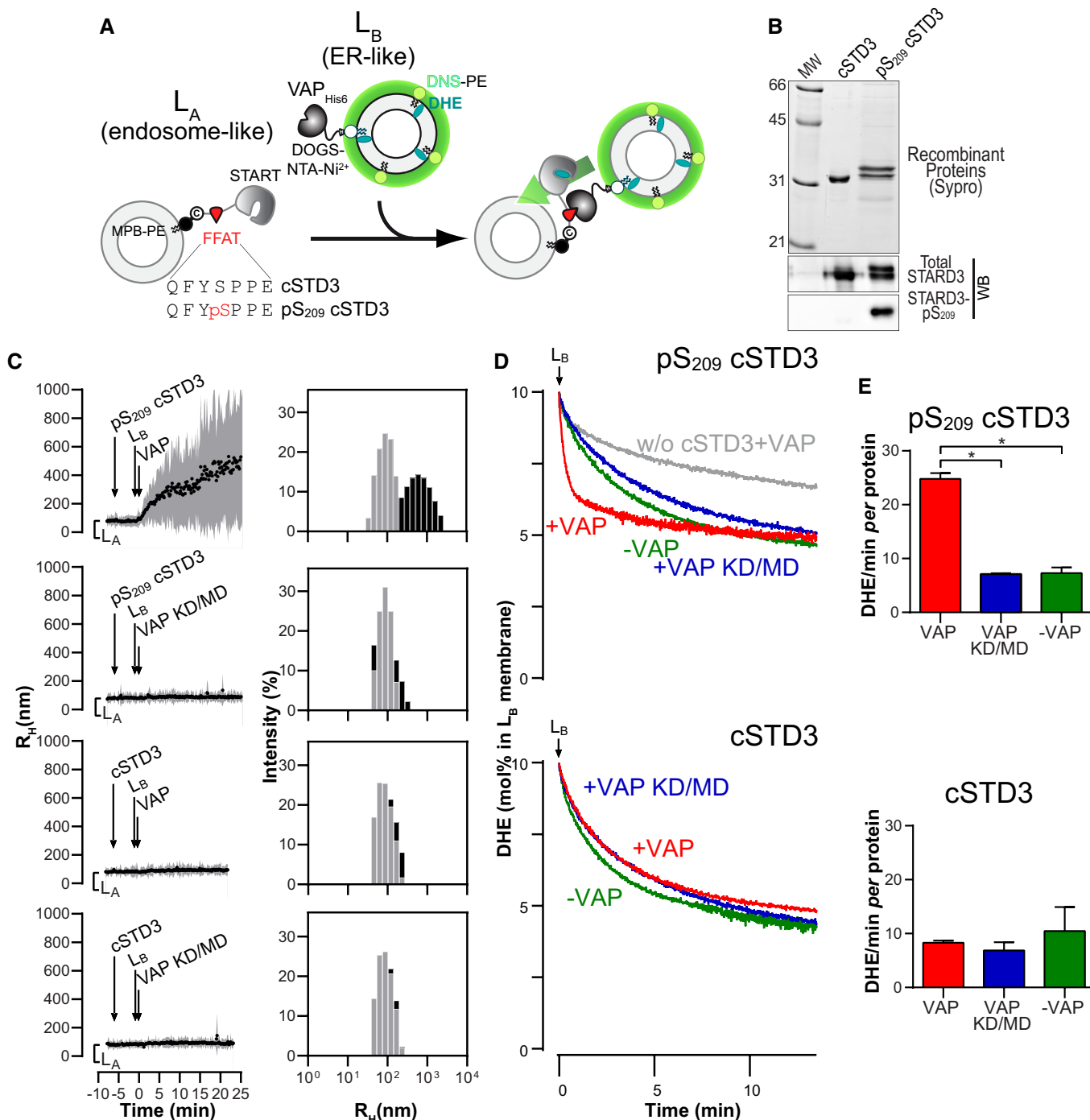


Figure 5.

Figure 5. Phosphorylation of STARD3 in its Phospho-FFAT motif governs membrane attachment and cholesterol transfer in *in vitro* reconstitution assays.

- A Description of the experimental strategy. L_A liposomes (endosome-like) are decorated with cSTD3 or pS₂₀₉ cSTD3 owing to covalent links with MPB-PE (1,2-dioleoyl-*sn*-glycero-3-phosphoethanolamine-N-[4-(*p*-maleimidophenyl) butyramide]), and mixed with L_B liposomes (ER-like) covered by VAP-A_{His6} attached to DOGS-NTA-Ni²⁺ (1,2-dioleoyl-*sn*-glycero-3-[(N-(5-amino-1-carboxypentyl) iminodiacetic acid) succinyl], nickel salt). For dehydroergosterol (DHE) transport experiment, L_B liposomes also contain DHE and a dansyl-phosphatidylethanolamine (DNS-PE). The transport of DHE from L_B to L_A liposomes is followed by measuring the change in FRET from DHE to DNS-PE.
- B SDS-PAGE gel and Western blot analysis of purified cSTD3 and pS₂₀₉ cSTD3 proteins. Top: The gel was stained with SYPRO Orange to visualize proteins and molecular weight markers. Bottom: Two similar gels were blotted onto nitrocellulose and analyzed for the presence of total and STARD3-pS₂₀₉ using specific antibodies.
- C Aggregation assays. L_A liposomes (50 μ M total lipids) were incubated for 5 min with cSTD3 or pS₂₀₉ cSTD3 (380 nM). Then, L_B liposomes (50 μ M total lipids) and VAP-A_{His6} or VAP-A KD/MD_{His6} (700 nM) were successively added. *Left panels*: mean radius (black dots) and polydispersity (shaded area) over time. *Right panels*: size distribution before (gray bars) and after the reaction (black bars).
- D DHE transport assay. DOPC (1,2-dioleoyl-*sn*-glycero-3-phosphocholine) liposomes (62.5 μ M total lipids, L_A) containing 3 mol% MPB-PE were mixed with cSTD3 or pS₂₀₉ cSTD3 (475 nM). After 5 min, liposomes (DOPC/DOGS-NTA-Ni²⁺/DNS-PE/DHE liposomes 77.5/10/2.5/10 mol/mol, 62.5 μ M total lipids, L_B), covered or not with 1 μ M of VAP-A_{His6} or VAP-A KD/MD_{His6}, were added. FRET between DHE and DNS-PE in the L_B liposomes diminishes as DHE is transported toward L_A liposomes. The signal was converted into amount of DHE present in L_B liposomes (in mol%).
- E Initial DHE transport rate measured with cSTD3 or pS₂₀₉ cSTD3 in the presence or absence of VAP-A_{His6} or VAP-A KD/MD_{His6}. Data are represented as mean \pm SEM ($n = 3$ for cSTD3-VAP and $n = 4$ for all other data). Mann-Whitney test (* $P < 0.05$).

Source data are available online for this figure.

MOSPD2 interacts with conventional and Phospho-FFAT motifs

We recently identified the MOSPD2 protein as a third member of the VAP family (Di Mattia *et al.*, 2018). To study more precisely the binding characteristics of MOSPD2 with Phospho-FFAT motifs, we produced in *E. coli* and purified the MSP domain of MOSPD2 (Fig 7A). Next, the recombinant MSP domain of MOSPD2 was incubated with streptavidin beads coupled to biotinylated peptides as described before for VAP. Bound proteins were eluted and analyzed by SDS-PAGE followed by Coomassie Blue staining (Fig 7B). Similarly to VAPs, the MSP domain of MOSPD2 interacted with the FFAT of STARD3 phosphorylated on S₂₀₉, and not with the unphosphorylated peptide (Fig 7B). We used SPR to determine the interaction dissociation constants between the different peptides and the MSP domain of MOSPD2. The concentrations used to determine affinities corresponded to a monomer for MOSPD2 since the recombinant MSP domain of the protein is monomeric (Di Mattia *et al.*, 2018). The kinetic profiles of the MSP domain of MOSPD2 were similar to those of VAPs (Fig 7C and D). Phosphorylation, on S₂₀₉ was mandatory, and additional phosphorylation increased the binding affinity (from $1.1 \pm 0.3 \mu$ M for pS₂₀₉, to $0.35 \pm 0.16 \mu$ M for pS₂₀₉ + pS₂₁₃ for instance) (Fig 7E). Interestingly, the affinity for a conventional FFAT was similar for MOSPD2, VAP-A, and VAP-B, as previously reported (Di Mattia *et al.*, 2018), while MOSPD2 had a slightly higher affinity for Phospho-FFAT compared to VAP-A and VAP-B (Figs 3E and 7E, and EV3E). Together, these data show that MOSPD2 interacts in the micromolar affinity range with the Phospho-FFAT motif only when its 4th residue is phosphorylated.

We characterized the interaction between a Phospho-FFAT and MOSPD2 *in vivo*. To do so, we immunoprecipitated GFP-tagged MOSPD2 from cells co-expressing the wild-type and mutant STARD3 proteins (Fig 7F). Wild-type STARD3 was co-immunoprecipitated with MOSPD2. In contrast, the non-phosphorylatable STARD3 mutant S₂₀₉A was not co-precipitated (Fig 7F). We showed before that the single phosphomimetic mutation S₂₀₉D was not sufficient to restore the interaction between STARD3 and VAP-A or VAP-B, while the double-mutation S₂₀₉D/P₂₁₀A restored binding (Fig 4A and B). MOSPD2 behaved differently: It associated, yet only moderately, with the single S₂₀₉D mutant, and almost not with the S₂₀₉D/P₂₁₀A double mutant (Fig 7F); one reason could be that the tridimensional

structure of the MSP domain of MOSPD2 differs from the one of VAPs.

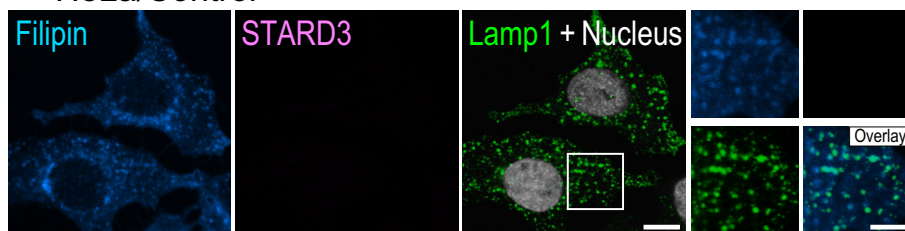
We next addressed whether in cells MOSPD2 was forming contact sites when co-expressed with STARD3. We imaged MOSPD2 recruitment on endosomes. Since the phosphomimetic mutant of STARD3 could not fully restore the interaction *in vitro*, we only tested the effect of the non-phosphorylatable mutant STARD3 S₂₀₉A (Fig 7I). Consistently, while wild-type STARD3 expression induced a strong enrichment of MOSPD2 around endosomes, MOSPD2 remained evenly distributed along the whole ER in the presence of the STARD3 S₂₀₉A mutant (Fig 7G–J). Similarly, MOSPD2 with the R404D/L406D double mutation (named RD/LD), which is defective in binding FFAT motifs, remained uniformly localized in the ER (Fig 7J).

Together, these data showed that the interaction of the MSP domain of MOSPD2 with the Phospho-FFAT motif depends on the critical phosphorylation of its central serine (S₂₀₉ in STARD3), similarly to the MSP domain of VAP-A and VAP-B. They also unveiled specific features of MOSPD2 in terms of affinity and mode of interaction.

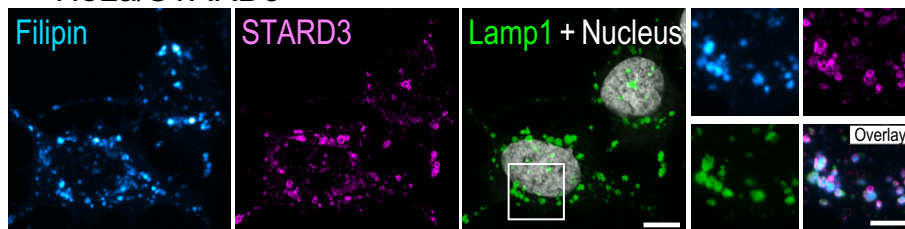
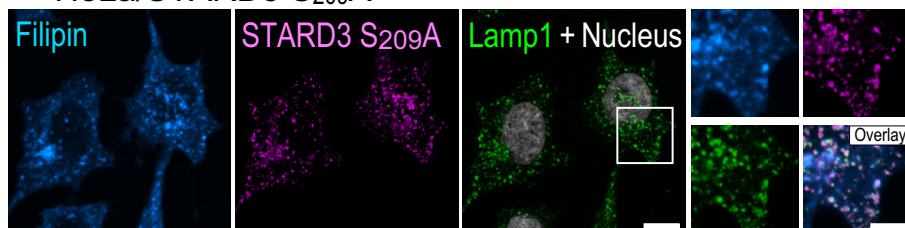
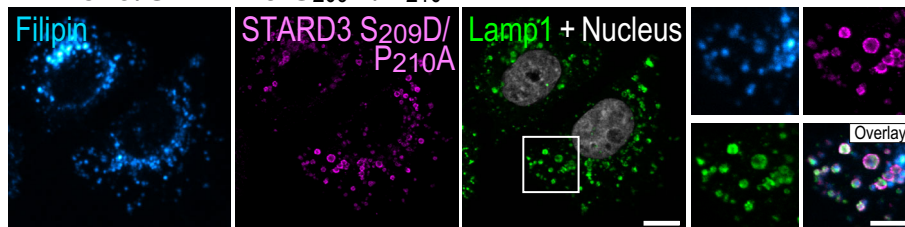
Structural characterization of the MSP domain of MOSPD2 in complex with a conventional FFAT and a Phospho-FFAT

The 3D structure of the MSP domain of human MOSPD2 was not characterized. Moreover, interactions studies presented before suggest that structural differences may exist between MOSPD2 and VAP MSP domains. To document the binding mode of MOSPD2 with the two types of FFAT motif, we solved the structure of the MSP domain of MOSPD2 unbound (PDB ID: 6TQT) (Fig 8A), and in complex with peptides corresponding to a conventional FFAT (ORP1) (PDB ID: 6TQS) (Fig 8B) and a Phospho-FFAT (STARD3) (PDB ID: 6TQU) (Fig 8C). The structure of the unbound state of the domain was resolved to 1.5 Å. The structure was broadly similar to that of rat VAP-A (PDB ID: 1Z9L; (Kaiser *et al.*, 2005); rmsd of 2.382 Å over 104 C α s). The main differences are seen in a flexible loop (residues 337–346 in human MOSPD2, residues 24–33 in VAP-A), and in the α -helix, which contains an extra turn at the N-terminal in MOSPD2. Besides, sequence analyses show that the residues that are conserved between VAPs and MOSPD2 are mostly found in

A HeLa/Control



B HeLa/STARD3

C HeLa/STARD3 S₂₀₉AD HeLa/STARD3 S₂₀₉D/P₂₁₀A

E HeLa/STARD3 Conv-FFAT

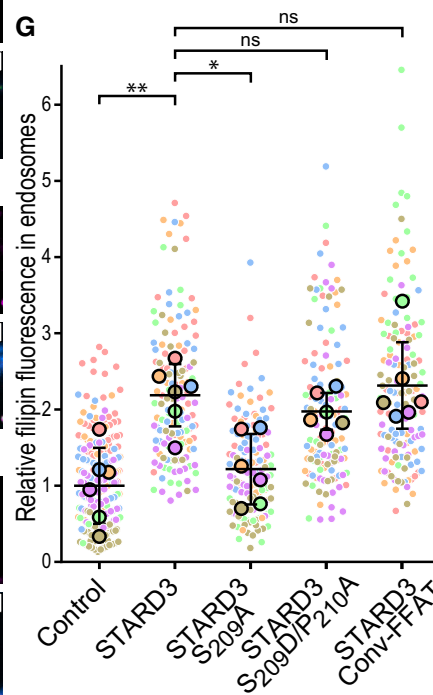
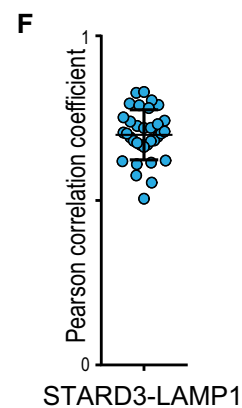
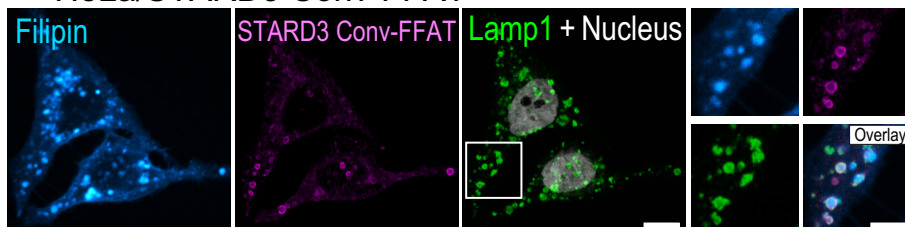


Figure 6. STARD3-mediated cholesterol transport in endosomes depends on S₂₀₉.

A–E HeLa/Control (A), HeLa/STARD3 (B), HeLa/STARD3 S₂₀₉A (C), HeLa/STARD3 S₂₀₉D/P₂₁₀A (D), and HeLa/STARD3 Conv-FFAT (E) cells were labeled with anti-STARD3 antibodies (magenta), anti-Lamp1 antibodies (green) and with the fluorescent cholesterol probe filipin (Cyan Hot). Nuclei are shown in gray (TO-PRO-3). Higher magnification images (2×) of the area outlined in white are shown on the right. The filipin, STARD3, and Lamp1 merged image is labeled Overlay. Scale bars: 10 μm. Inset scale bars: 5 μm.

F Pearson's correlation coefficients between STARD3 and Lamp1 staining in HeLa/STARD3 cells. Each dot represents a single cell (34 cells from 4 independent experiments). Mean and error bars (SD) are shown. Note that STARD3 and Lamp1 signals are highly correlated.

G Relative fluorescence intensity of intracellular filipin signals in endosomes of HeLa/Control, HeLa/STARD3, HeLa/STARD3 S₂₀₉A, HeLa/STARD3 S₂₀₉D/P₂₁₀A, and HeLa/STARD3 Conv-FFAT cells. Data are displayed as a Superplot (Lord *et al*, 2020) showing the relative filipin fluorescence intensity in endosomes of individual cells (small circles) from 6 independent experiments (mean of each experiment shown as a large circle). Independent experiments are color-coded. Means and error bars (SD) are shown as black bars. Kruskal–Wallis with Dunn's multiple comparison test (**P* < 0.05; ***P* < 0.01; *n* = 6 independent experiments).

the region which interacts with FFATs (Appendix Fig S5). In this binding interface, two main differences are present: (i) An asparagine and a serine are swapped between the VAP proteins and

MOSPD2: N64 and S65 in VAP-A (N57 and S58 in VAP-B) are replaced with S377 and N378 in MOSPD2, respectively; (ii) K52 in VAP-A is replaced with an arginine, R365.

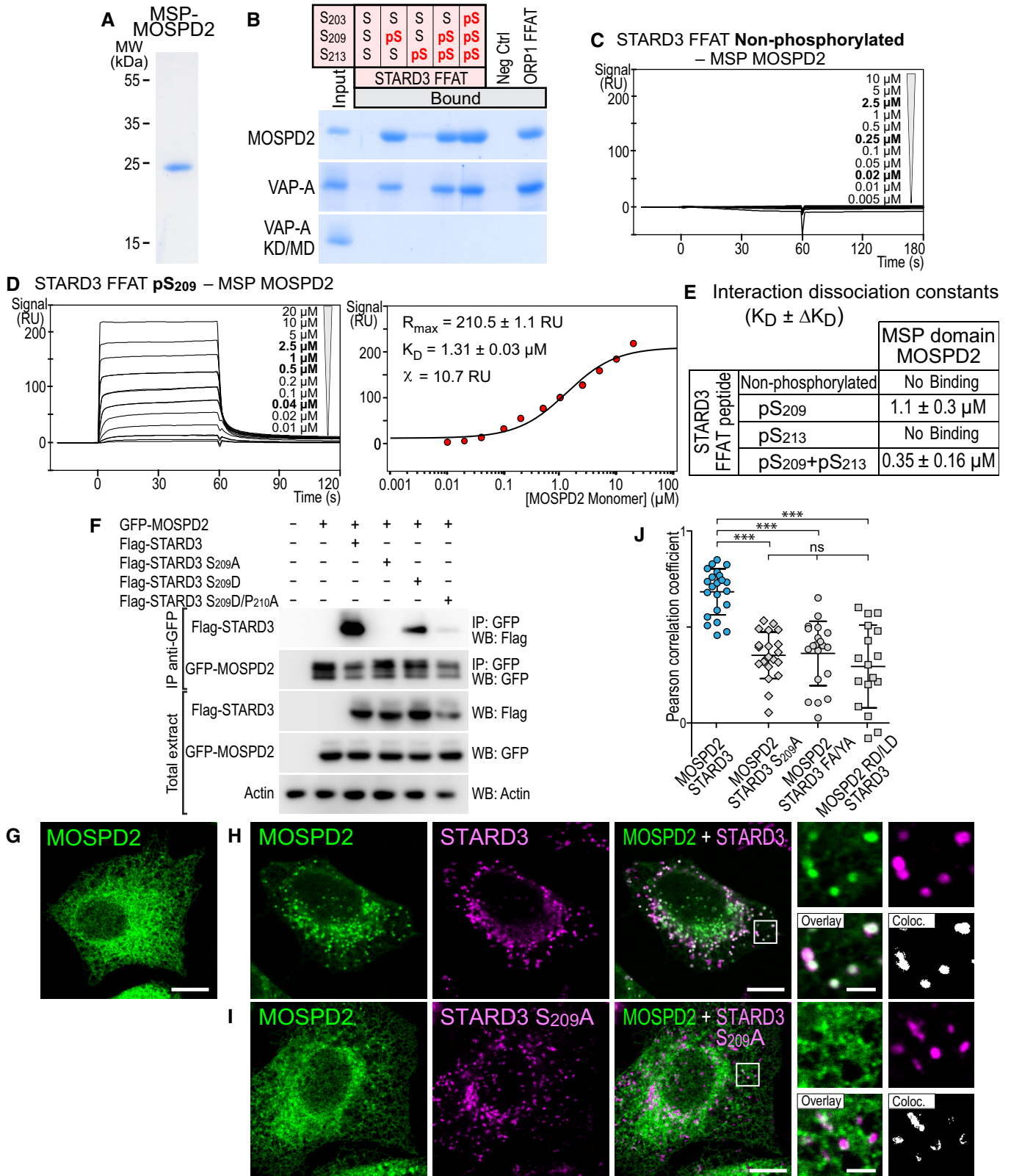


Figure 7.

Figure 7. MOSPD2 interacts with the Phospho-FFAT motif in a phosphorylation-dependent manner.

- A Coomassie Blue staining of the recombinant MSP domain of MOSPD2 after SDS-PAGE.
- B Recombinant MSP domains pulled down with STARD3 FFAT (unphosphorylated, monophosphorylated on S₂₀₉ or S₂₁₃, bi-phosphorylated on S₂₀₉ and S₂₁₃, or tri-phosphorylated on S₂₀₃, S₂₀₉ and S₂₁₃) and control peptides were revealed by Coomassie Blue staining. The recombinant proteins subjected to the assay are shown in the input fraction.
- C, D SPR analysis of the MSP domain of MOSPD2 binding onto immobilized unphosphorylated (C) and pS₂₀₉ (D) STARD3 FFAT. Representative sensorgrams resulting from the interaction between the MSP domain of MOSPD2 injected at different concentrations and the different FFAT peptides are shown in (C) and (D left). Binding curves display the SPR signal (RU) as a function of time. Concentrations printed in bold indicate samples measured twice. Signal obtained for the negative control peptide immobilized on another flow cell is systematically subtracted, as well as the bulk effect recorded with buffer only. (D right) Steady-state analysis of the interaction between pS₂₀₉ STARD3 FFAT peptide and the MSP domain of MOSPD2. Equilibrium responses (R_{eq}) extracted from the left panel were plotted as a function of the monomeric concentration of the MSP domain of MOSPD2, and fitted with a 1:1 binding model. The experiments were performed at 25°C in 50 mM Tris-HCl pH 7.5, 75 mM NaCl buffer supplemented with 0.005% (v/v) surfactant polysorbate 20 (P20, GE Healthcare). Mean of 2 independent experiments. Uncertainties are obtained from the standard deviation considering a *t*-distribution coefficient for a risk factor of 32%.
- E Interaction dissociation constants between the different STARD3 FFAT peptides and the MSP domain of MOSPD2.
- F Immunoprecipitation (GFP-Trap) experiments between GFP-tagged MOSPD2 and Flag-tagged STARD3 (WT and S₂₀₉A, S₂₀₉D, and S₂₀₉D/P₂₁₀A mutants). Approximately 5 µg of total protein extract was analyzed by Western blot using anti-Flag, anti-GFP and anti-Actin antibodies. Immunoprecipitated material was analyzed using anti-Flag and anti-GFP antibodies.
- G-I GFP-MOSPD2-expressing cells (green) were untransfected (G), transfected with Flag-STARD3 (H) and Flag-STARD3 S₂₀₉A (I), and labeled using anti-Flag (magenta) antibodies. The subpanels on the right are higher magnification (3.5×) images of the area outlined in white. The Overlay panel shows merged green and magenta images. The Coloc panel displays a colocalization mask on which pixels where the green and the magenta channels co-localize are shown in white. Scale bars: 10 µm. Inset scale bars: 2 µm.
- J Pearson's correlation coefficients between MOSPD2 (WT or RD/LD) and STARD3 (WT, S₂₀₉A, or FA/YA) staining are shown. Each dot represents a single cell (number of cells: MOSPD2-STARD3: 22; MOSPD2-STARD3 S₂₀₉A: 21; MOSPD2-STARD3 FA/YA: 20; MOSPD2 RD/LD-STARD3: 17, from at least three independent experiments). Means and error bars (SD) are shown. Kruskal-Wallis with Dunn's multiple comparison test (***) *P* < 0.001.

Source data are available online for this figure.

The 3D structure of the MSP domain of rat VAP-A and human MOSPD2 bound with the conventional FFAT motif of ORP1 (Fig 8D) are similar. Superposition of the domains showed a few changes in the binding interface, with almost all contacts being maintained. Since N64 in VAP-A is replaced with S377 in MOSPD2, the direct hydrogen bond between the side chain of N64 and the main chain carbonyl of A₄₇₉ in the peptide is replaced with a water-mediated contact. K52 in VAP-A is replaced with R365, which makes a hydrogen bond with D₄₇₈ of the peptide (Fig 8E).

However, a different picture is seen when comparing the structures of human VAP-A and MOSPD2 bound to the phosphorylated FFAT of STARD3 (Fig 8F and G). In the MOSPD2 complex, residues corresponding to the 5th and 6th positions of the phospho-FFAT (P₂₁₀ and P₂₁₁) maintain broadly similar orientations than their cognate residues in the conventional FFAT (A₄₇₉ and L₄₈₀). However, a hydrogen bond cannot be maintained between P₂₁₀ of the Phospho-FFAT and the carbonyl of V364 of the MSP domain. In the conventional FFAT, a water-mediated contact exists between the amide of position 6 (L₄₈₀ in ORP1) and the carbonyls of P369 and Y372 in the MSP domain. These contacts, again, cannot be maintained with the Phospho-FFAT where a proline is in position 6 of the motif (Fig 8J). Another difference is that more residues carboxyl-terminal to the FFAT core sequence can be seen bound to the MSP domain in MOSPD2 than in VAP-A. This can be explained by specific MOSPD2 features. Firstly, as previously noted, N64 in human VAP-A is replaced with S377 in MOSPD2. This shorter side chain allows the carbonyl and amide of pS₂₁₃ one residue after the end of the phosphorylated FFAT motif to form hydrogen bonds with the amide and hydroxyl of S377. The larger side chain of N64 in VAP-A would prevent these contacts from forming. Secondly, MOSPD2 possesses one extra turn at the N-term of the α -helix, which creates a hydrophobic pocket composed of N378, P420, L423, and T424 into which F₂₁₄, two residues after the FFAT motif of

STARD3, can bind (Fig 8I). The lack of this extension in VAP-A and N378 being replaced by S65 in VAP-A would prevent a hydrophobic residue from binding here. It should be noted that contacts between pS₂₁₃ and F₂₁₄ are only maintained in one copy of the complex in our structure. In the second copy, F₂₁₄ makes crystal contacts with a symmetry-related molecule.

Finally, the structural differences seen between the unbound and complexed forms of VAP-A are not seen between the unbound and complexed forms of MOSPD2, with F405 (F95 in VAP-A) maintained in the same position as in the complexed form of VAP-A. M96 in human VAP-A is replaced in MOSPD2 with a leucine, L406, in the tp rotamer, similar to the conformation of M96 in complexed VAP-A (Fig 8H).

We next assessed whether K363 in MOSPD2, which is at the same position as K50 in VAP-A and K43 in VAP-B, had a predominant role in binding the Phospho-FFAT. K363 of MOSPD2 was mutated in leucine (K363L mutant), and the interaction of the mutant protein with the different peptides was assessed. While this mutation abolishes binding of Phospho-FFATs in VAP-A and VAP-B, the same mutation in MOSPD2 (K363L) only partially affected the binding of both the conventional and the Phospho-FFAT motif (Fig EV2A).

Altogether these structural and functional data show that MOSPD2 binds conventional and Phospho-FFAT on a similar interface as VAP-A, but MOSPD2 has unique and specific features which increase the binding interface, in particular a hydrophobic pocket binding the 9th residue of the FFAT motif.

Discussion

Distinct organelles are physically attached by membrane contact sites (Loewen *et al*, 2003; Wu *et al*, 2018). These connections must

be reversible, because it is known that organelles associate and dissociate over time (Friedman *et al*, 2011, 2013; Valm *et al*, 2017). Such dynamics imply that there are molecular mechanisms

controlling association and dissociation (Alli-Balogun & Levine, 2019). The ER makes physical connections with nearly all organelles (Balla *et al*, 2019). To date, no clear molecular mechanism was

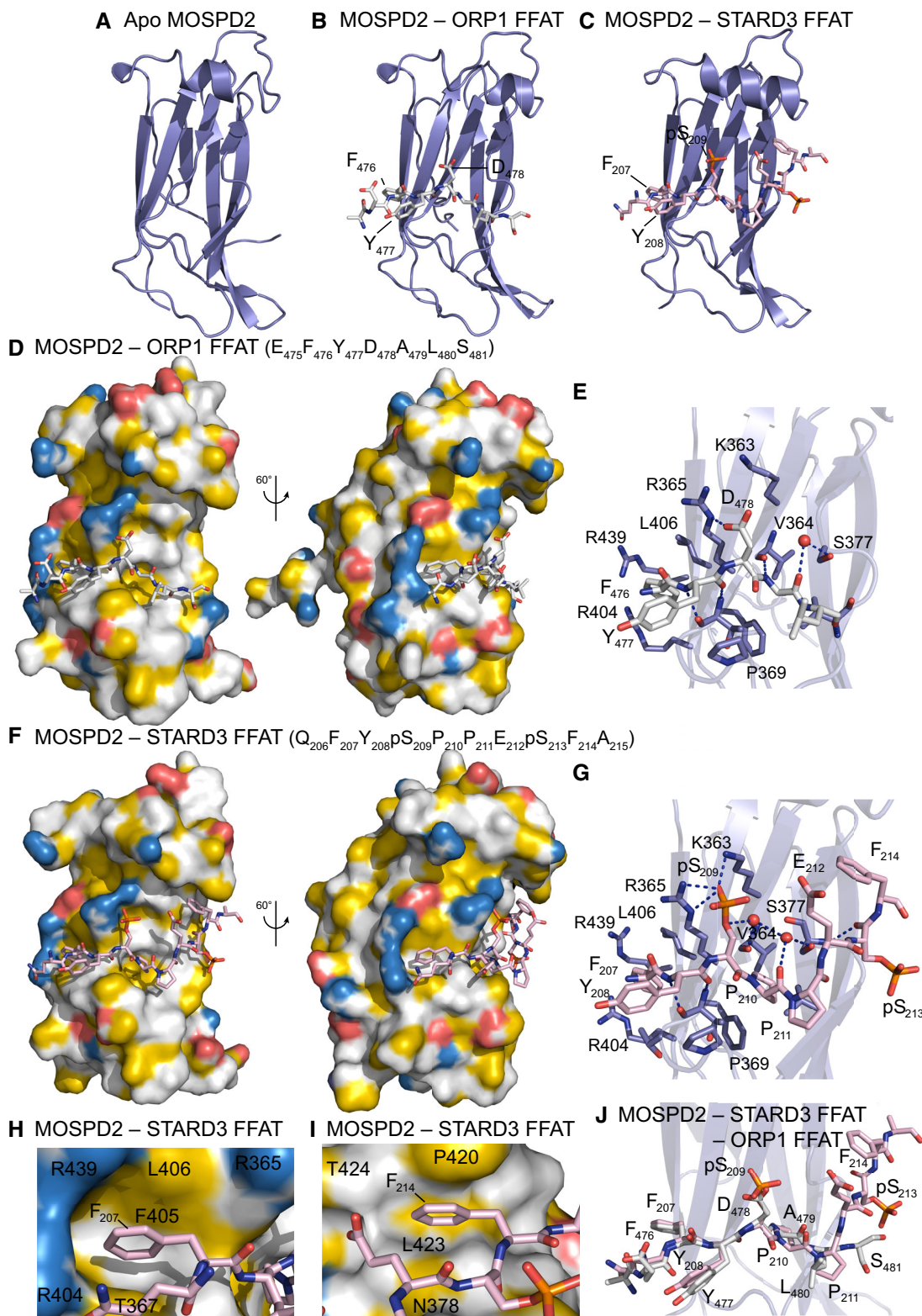


Figure 8.

Figure 8. Structure of the MSP domain of MOSPD2 in its unbound form, and in complex with a conventional FFAT and a Phospho-FFAT.

- A–C Ribbon diagram of the MSP domain of MOSPD2 in its unbound form (A), in complex with the conventional FFAT of ORP1 (B), and in complex with the Phospho-FFAT of STARD3 (C).
- D Surface representation of the MSP domain of MOSPD2 in complex with the conventional FFAT of ORP1.
- E Close-up view of the structure near the conventional FFAT motif highlighting critical residues (in stick model) of human MOSPD2 present in the binding interface.
- F Surface representation of the MSP domain of MOSPD2 in complex with the phosphorylated FFAT of STARD3.
- G Close-up view of the structure near the Phospho-FFAT motif highlighting critical residues (in stick model) of human MOSPD2 present in the binding interface.
- H, I Close-up view of the hydrophobic pockets interacting with the 2nd residue (F₂₀₇) (H) and the 9th residue (F₂₁₄) (I) of the Phospho-FFAT of STARD3; residues of MOSPD2 constituting the pockets are indicated.
- J Superposition of the structures shown in (E) and (G) showing the similar trajectories of the peptides.

Data information: Phosphorous, nitrogen, and oxygen atoms are colored in orange, blue, and red, respectively. Carbon atoms are shown in slate blue, gray, and rose in the MSP domain, the conventional FFAT motif, and the Phospho-FFAT motif, respectively. (D, F, H, I): The protein surface is colored according to the YRB scheme, showing hydrophobic, negatively and positively charged atoms in yellow, red, and blue, respectively; the other atoms are in white (Hagemans *et al*, 2015). (E, G): Red spheres are water molecules.

reported to explain a controlled and/or reversible association, except for the yeast mitochondria-vacuole contacts which were shown to be disrupted by phosphorylation of Vps39 (Hönscher *et al*, 2014). In our study, we focused on contacts made by the ER and other organelles. The ER uses VAP-A/VAP-B/MOSPD2, three distinct membrane-bound proteins, as receptors on its surface to bind proteins from other organelles (Murphy & Levine, 2016; Di Mattia *et al*, 2018). The interaction between VAP-A/VAP-B/MOSPD2 and their partners allows the formation of contacts between the ER and the other organelles of the cell, by binding a short linear motif, named FFAT, present in protein partners that are attached or integral to other organelle membranes. This single molecular mechanism explains a large part of the formation of contact sites with the ER. How these are controlled remains unclear.

Many proteins binding to VAP-A/VAP-B/MOSPD2 have been identified over the last years (Huttlin *et al*, 2015; Murphy & Levine, 2016; Di Mattia *et al*, 2018). A number of these proteins do not have a conventional FFAT motif; however, their sequences suggested the presence of another kind of FFAT motif that could be activated by phosphorylation, that we defined here as a Phospho-FFAT motif. The presence of a phosphorylatable serine/threonine residue at a key position of the motif supported the idea that phosphorylation governs the interaction with VAP-A/VAP-B/MOSPD2. Moreover, the presence of a phosphorylatable residue within the core motif would serve as a reversible switch for forming contact sites. Modifying the FFAT search algorithm into a Phospho-FFAT search one allowed the identification of many candidate proteins in the human proteome. Interestingly, by crossing the list with proteomics data, we found that Phospho-FFAT motifs are as equally distributed as conventional FFAT motifs. In addition, both motifs coexist in about half of the candidates. Taking the complex formed by STARD3 and VAP-A/VAP-B/MOSPD2 as a model, we functionally characterized Phospho-FFAT motifs. We showed that in the absence of phosphorylation, the motif is not recognized by VAP-A/VAP-B/MOSPD2; phosphorylation on the 4th residue switches the motif on and allows its recognition by VAP-A/VAP-B/MOSPD2, triggering the formation of ER-endosome contact and enabling cholesterol transfer (Fig 9).

Phosphorylation modifies the chemical properties of a protein, modulating its charge (phosphorylated serine contains two negative charges at physiological pH), and sometimes its shape. The FFAT motif was defined as a core sequence flanked by an acidic tract. These adjacent D/E residues bear negative charges that are crucial

during the process of recognition of the FFAT sequence by the MSP domain. Nuclear magnetic resonance studies revealed that the interaction of the FFAT with the MSP domain occurs in two steps (Furuita *et al*, 2010): First, the acidic residues make non-specific electrostatic interactions with the electropositive surface of the MSP domain. Then, this intermediate complex is stabilized by specific interactions, notably by the phenylalanine in the 2nd position of the FFAT core. Most importantly, higher numbers of negative charges (including phosphorylation) in the acidic tract, by affecting the formation of the intermediate complex, increase the apparent binding affinity of the MSP domain for the FFAT motif (Furuita *et al*, 2010). This was demonstrated for STARD11 (also known as CERT) which is phosphorylated on S₃₁₅ located in the acidic tract of its conventional FFAT motif. Phosphorylation of this serine enhances the interaction with VAP and favors its ceramide transport activity in ER-Golgi contacts (Kumagai *et al*, 2014). In the case of STARD3, we found that the kinetics of sterol transport *in vitro* were similar when the START domain of STARD3 was associated with a conventional FFAT motif (Wilhelm *et al*, 2017), or with its own Phospho-FFAT motif bearing a single phosphorylation on the fourth core residue S₂₀₉. We can then speculate that in the case of STARD3, additional phosphorylations in the vicinity of the Phospho-FFAT could increase the speed of sterol transport; unfortunately, we could not test this as the production in *E. coli* of the protein with several phosphorylated serines was unsuccessful. However, we did show that additional phosphorylations, such as the one on S₂₁₃, increase the affinity of VAP for the FFAT motif. Thus, phosphorylations are involved in two different types of regulation: Phosphorylation can act as a switch to turn on and off the interaction, and it can act as a modulator to increase the affinity between VAP-A/VAP-B/MOSPD2 and their partners, and possibly fine-tune the function of the complex. An opposite function of phosphorylation on the FFAT motif can be envisaged; indeed, a phosphomimetic residue replacing the serine at position 5 of the FFAT of AKAP220 protein was shown to inhibit the binding to VAPs, which is consistent with the existence of an inhibitory role of phosphorylation on serines/threonines at position 5 of the motif (Mikitova & Levine, 2012).

Proteins involved in inter-organelle contacts have targeting determinants enabling their association with separate organelles (Alli-Balogun & Levine, 2019). Thus, the regulation of these targeting determinants can theoretically modulate MCS formation. For instance, OSBP is targeted to the Golgi by the affinity of its PH

at position 5. However, an even more striking difference is found in MOSPD2 which forms a second hydrophobic pocket accommodating an aromatic residue (F_{214}) of the Phospho-FFAT of STARD3. This pocket most probably binds hydrophobic residues present in position +9 of some FFAT motifs and might account for the stronger affinity of FFATs with this feature for MOSPD2 compared to VAP-A/B.

VAP-A and VAP-B are more closely related to each other (82% identity; 93% similarity) than they are to MOSPD2 (~30% identity and ~50% similarity between VAPs and MOSPD2). Our finding that some FFAT-containing proteins interact with VAP-A/B but not with MOSPD2 raises the possibility that the repertoires of proteins bound by these receptors are not identical; some FFATs likely bind the three receptors, while others may have a better affinity or a selectivity for one or the other. This is expected because MOSPD2 appeared more recently than VAP during evolution, and is only found in metazoans. Comparative proteomics studies will be required to make an inventory of the partner repertoires of these three proteins.

Overall, this study shows that the formation of MCSs by VAP-A/VAP-B/MOSPD2 can be switched on and off by phosphorylation of some of their partners. This mechanism makes contact formation controllable through signaling. Such a regulation by phosphorylation of Phospho-FFATs could originate through direct signaling in response to extracellular or intracellular signals, or indirectly via transcription. The kinases and phosphatases regulating this process, as yet unknown, will most probably be different depending on their primary target, i.e., the partner of VAP-A/VAP-B/MOSPD2. The identification of kinases and phosphatases switching on and off Phospho-FFATs is the next step to understand how these regulatory processes are integrated in the cell.

Materials and Methods

Cloning and constructs

The GFP-VAP-A (WT and KD/MD mutant), GFP-VAP-B (WT and KD/MD mutant), GFP-MOSPD2 (WT and RD/LD mutant), Flag-tagged STARD3, STARD3 FA/YA, and GST-tagged STARD3 expression vectors were previously described (Alpy *et al.*, 2005, 2013; Di Mattia *et al.*, 2018). STARD3 S_{209A} , STARD3 S_{209D} , STARD3 S_{209D}/P_{210A} , and STARD3 Conv-FFAT were constructed by site-directed mutagenesis using the following primers: STARD3 S_{209A} : 5'-GACAG TTCTA TGCAC CCCCA GAATC CTTTG C-3' and 5'-GATTC TGGGG GTGCA TAGAA CTGTC CCTCG G-3'; STARD3 S_{209D} : 5'-GACAG TTCTA TGATC CCCCA GAATC CTTTG C-3' and 5'-GATTC TGGGG GATCA TAGAA CTGTC CCTCG G-3'; STARD3 S_{209D}/P_{210A} : 5'-TTCTA TGATG CCCCA GAATC CTTTG CAGGG TCTGA CAAT-3' and 5'-TTCTG GGGCA TCATA GAACT GTCCC TCGGA CAGAG CACC-3'; STARD3 P_{210A} : 5'-TTCTG GGGCT GAATA GAACT GTCCC TCGGA CAGAG CACCG GAG-3' and 5'-TTCTA TTCAG CCCCA GAATC CTTTG CAGGG TCTGA CAATG AATC-3'; STARD3 Conv-FFAT: 5'-CCGGT GCTCT GGACG ATGAA GAGTT CTTTG ATGCC TCAGA ATCCT TTGCA GGGTC TGACA ATG-3' and 5'-AAAGG ATTCT GAGGC ATCAA AGAAC TCTTC ATCGT CCAGA GCACC GGAGA ACAGC AGGGG TCC-3'. The cDNA encoding STARD3 insensitive to siRNAs was obtained by gene synthesis (GenScript); silent mutations were introduced in the four sequences targeted by

STARD3 siRNAs (SMARTpool ON-TARGETplus L-017665-00, Horizon Discovery).

Plasmids allowing the inducible expression of STARD3 were constructed in the lentiviral vector pLVX-TRE3G (Clontech) using the following primers: 5'-TCCGG GCCCG CGGCC GCCAC CATGA GCAAG CTGCC CAGGG AGCTG-3' and 5'-CTACC CGGTA GAATT TCACG CCCGG GCCCG CAGCT CGCT-3' with the SLiCE method (Okegawa & Motohashi, 2015).

Plasmids encoding the MSP domain of VAP-A (8–212; WT and KD/MD mutant), VAP-B (1–210; WT and KD/MD mutant), and MOSPD2 (282–490; WT and RD/LD mutant) for expression as C-terminal His6-tag proteins in *E. coli* were previously described (Mesmin *et al.*, 2013; Wilhelm *et al.*, 2017; Di Mattia *et al.*, 2018). VAP-A K50L, VAP-B K43L, and MOSPD2 K363L were constructed by site-directed mutagenesis using the following primers: VAP-A K50L: 5'-AGAAA AGTGT GTTTC CTAGT GAAGA CTACA GCACC TCGCC GGTAC TGT-3' and 5'-GCGAG GTGCT GTAGT CTTCA CTAGG AAACA CACTT TTCTA TCCGA TGG-3'; VAP-B K43L: 5'-CGAAA TGTGT GTTTT CTAGT GAAGA CTACA GCACC ACGTA GG-3' and 5'-TGCTG TAGTC TTCAC TAGAA AACAC ACATT TCGGT CTGTC GG-3'; MOSPD2 K363L: 5'-GGAGC TGTTG TTCTC ACCAG AAATG CCACT ATATT TTTAG TTA-3' and 5'-TAACT AAAAA TATAG TGGCA TTTCT GGTGA GAACA ACAGC TCC-3'. For protein crystallization, a plasmid encoding MOSPD2 (315–445) fused to an N-terminal His6-tag followed by a thrombin cleavage site was generated.

A plasmid encoding STARD3 (196–445) with a cysteine substitution (L_{196C}) to link the soluble part of STARD3 to MPB-PE containing liposomes, and fused with an N-terminal GST tag for purification, was generated. The protein encoded by this construct (without GST) is hereafter referred to as cSTD3. To obtain the p S_{209} cSTD3 encoding construct, the S_{209} codon was replaced by an amber codon (TAG) by site-directed mutagenesis using the following primers 5'-GGACA GTTCT ATTAG CCCCC AGAAT CCTTT GCAGG G-3' and 5'-GGATT CTGGG GGCTA ATAGA ACTGT CCCTC GGACA G-3'. All constructs were verified by DNA sequencing (Eurofins).

Protein expression and purification

For recombinant MSP domains of VAP-A, VAP-B, and MOSPD2 (282–490), proteins were expressed in *E. coli* BL21 (DE3) strain at 20°C for 16 h upon induction with 1 mM IPTG (at an optical density $OD_{600nm} = 0.5$). Cells were suspended in lysis buffer [50 mM sodium phosphate pH 8.0, 300 mM NaCl, 10 mM imidazole, protease inhibitor tablets (cComplete, Roche)]. Cells were lysed by a Cell Disruptor TS SERIES (Constant Systems Ltd), and the lysate was first centrifuged at 3,500 g for 15 min, then at 50,000 g for 45 min, and filtered through a 0.22- μ m membrane. Purification was performed on an ÄKTA Start chromatography system (GE Healthcare Life Sciences) using HisTrap HP 1 ml columns. Proteins were eluted with Elution buffer [20 mM sodium phosphate pH 7.4, 250 mM imidazole], and further purified by gel filtration (HiLoad 16/60 Superdex 200, GE) in GF Buffer (20 mM Tris-HCl pH 7.5, 150 mM NaCl). Proteins were concentrated with an Amicon Ultra-15 10 kDa centrifugal filter unit (Merck). Protein concentration was determined by UV-spectroscopy.

For the recombinant MSP domain of MOSPD2 [315–445], purification was performed with NTA-Ni²⁺ agarose beads (HIS-Select

Nickel Affinity Gel, P6611, Sigma). The protein was first bound onto the column. After one washing step with lysis buffer, the His6-tag was removed to allow the release of MOSPD2 (315–445) by incubating the beads in digestion buffer (50 mM sodium phosphate pH 8.0, 300 mM NaCl, 10 mM imidazole, 25U thrombin, 50 μ M CaCl₂) for 16 h at 4°C, under constant agitation. After incubation, thrombin was inactivated by adding PMSF (200 mM). The protein was recovered in the supernatant after centrifugation, and the beads were washed three times with lysis buffer. The fractions were pooled. The protein was then purified by gel filtration (in GF buffer containing 1 mM TCEP), concentrated, and quantified as described above.

GST-pS₂₀₉ cSTD3 was expressed in the *E. coli* C321 Δ A strain [gift from George Church; Addgene # 48998 (Lajoie et al, 2013)] transformed with the phosphoserine orthogonal translation system SepOTS λ , a plasmid encoding a phosphoserine-accepting tRNA, a phosphoserine aminoacyl-tRNA synthetase to load the phosphoserine onto a UAG-decoding Phosphoserine-tRNA, and a modified elongation factor Tu (EF-Sep) to deliver phosphoserine-tRNA to the ribosome. These materials were gifts from Jesse Rinehart [Addgene # 68292, # 68306 (Pirman et al, 2015)]. Bacteria were cultivated in LB medium containing ampicillin (100 μ g/ml), kanamycin (25 μ g/ml), 0.08 % glucose, and 2 mM O-phospho-L-serine (P0878, Sigma), at 30°C for 20 h upon induction with 1 mM IPTG (at an optical density OD_{600nm} = 0.7). All purification steps were conducted in TN1 buffer (50 mM Tris-HCl pH 7.4, 150 mM NaCl) containing 2 mM DTT. TN1 buffer was supplemented with 1 mM PMSF, 10 μ M bestatin, 10 μ M pepstatin, 1 mM orthovanadate, 50 mM NaF, and protease inhibitor tablets (cOmplete, Roche) for the first purification steps. Cells were lysed by a Cell Disruptor TS SERIES, and the lysate was centrifuged at 186,000 g for 1 h. Then, the supernatant was applied to Glutathione Sepharose 4B beads (17-0756, GE Healthcare). After three washing steps with TN1 buffer containing 2 mM DTT, the beads were incubated with thrombin at 4°C for 16 h to cleave the GST fusion, and allow the release of pS₂₀₉ cSTD3. The protein was recovered in the supernatant after centrifugation, and the beads were washed three times with TN1 buffer. The fractions were pooled and concentrated. Stock concentration was estimated with a BCA assay. The day of the experiment, in order to attach pS₂₀₉ cSTD3 covalently to MPB-PE-containing liposomes, 100 μ l from stock protein was applied onto an illustra NAP-5 column (GE Healthcare) and eluted with freshly degassed TN1 buffer according to manufacturer's indications to remove DTT. The concentration of the eluted protein was determined by UV-spectroscopy.

GST-cSTD3 was expressed in *E. coli* BL21 (DE3) at 37°C for 3 h upon induction with 1 mM IPTG (at an optical density OD_{600nm} = 0.6). All purification steps were conducted in TN1 buffer containing 2 mM DTT. TN1 buffer was supplemented with 1 mM PMSF, 10 μ M bestatin, 10 μ M pepstatin, and protease inhibitor tablets (cOmplete, Roche) for the first purification steps. All the following steps of the purification are the same as GST-pS₂₀₉ cSTD3, in particular the application onto illustra NAP-5 column for the experiments.

Cell culture, transfection, and infection

HeLa cells [American Type Culture Collection (ATCC) CCL-2] were maintained in DMEM with 5% fetal calf serum (FCS) and 40 μ g/ml

gentamicin. 293T cells (ATCC CRL-3216) were maintained in DMEM with 10% FCS, penicillin 100 UI/ml, and streptomycin 100 μ g/ml. HCC1954 cells (ATCC CRL-2338) were maintained in RPMI w/o HEPES with 10% FCS and 40 μ g/ml gentamicin.

Cells were transfected using X-tremeGENE 9 DNA Transfection Reagent (Roche). To generate retroviral particles, pQCXIP vectors were co-transfected with pCL-Ampho vector (Imgenex) into 293T retroviral packaging cell line. Retroviral infections were used to generate HeLa/Ctrl, HeLa/GFP-VAP-A (WT and KD/MD mutant), HeLa/GFP-VAP-B (WT and KD/MD mutant), and HeLa/GFP-MOSPD2 (WT and RD/LD mutant) cell lines. The HeLa/Ctrl cell line was obtained using the empty pQCXIP plasmid. For lentiviral infection, pLVX-TRE3G vectors encoding STARD3 (wild-type and mutants) or pLVX-Tet3G vector encoding the transactivator were co-transfected with three packaging plasmids pLP1, pLP2, and pLP/VSVG (Invitrogen) into the 293T cell line. Viral particles supplemented with 10 μ g/ml polybrene and 20 mM HEPES were then incubated with HeLa cells. Selection was performed using 0.5 μ g/ml puromycin or 800 μ g/ml G418. siRNA transfections were performed using Lipofectamine RNAiMAX (Invitrogen) according to the manufacturer's instructions. Control siRNA (D-001810-10) and STARD3-targeting siRNAs (L-017665-00) were SMARTpool ON-TARGETplus obtained from Horizon Discovery.

Antibody production and purification

The anti-phospho-STARD3-pS₂₀₉ antibody (rabbit polyclonal antibody #3144) was raised against the synthetic peptide CDGQFYpSP-PESEA. The peptide was coupled to ovalbumin by its N-terminal cysteine residue, and injected in a rabbit. The immunoreactive serum was purified using a two-step protocol: First, the serum was loaded on an affinity chromatography column bearing the non-phosphorylated synthetic peptide (CDGQFYSPPESEA), and the unbound fraction was collected; second, this latter fraction was purified on an affinity chromatography column bearing the phosphorylated synthetic peptide, and the bound fraction was collected. In these experiments, peptides were coupled to SulfoLink Coupling Gel (Thermo Scientific Pierce) using conditions recommended by the manufacturer.

Peptide synthesis

Peptides were synthesized on an Applied Biosystems 433A peptide synthesizer using standard Fmoc chemistry, and purified by reverse phase HPLC using a preparative scale column (Phenomenex: Kinetex EVO C18, 100 A, 5 μ M, 250 \times 21.2 mm). Molecular weight and purity of the peptides were confirmed by mass spectrometry.

Peptide pull-down assays

For pull-down assays of whole cell protein extracts, the affinity resin was prepared by incubating 60 nmol of biotinylated peptide with 15 μ l of streptavidin beads (PureProteome Streptavidin Magnetic Beads, Merck) in a total volume of 1 ml pull-down buffer 1 (PDB1) [50 mM Tris-HCl pH 7.4, 75 mM NaCl, 1 mM EDTA, 1% Triton X-100, protease inhibitor tablet (cOmplete, Roche)] at 4°C for 1 h, under constant agitation. The beads were then washed twice with 1 ml of PDB2 [50 mM Tris-HCl pH 7.4, 500 mM NaCl, 1 mM EDTA, 1% Triton X-100, protease inhibitor tablets (cOmplete, Roche)], and

two times with 1 ml of PDB1. Adherent cells were washed two times with cold PBS (phosphate buffer saline) and lysed in PDB3 [50 mM Tris-HCl pH 7.4, 75 mM NaCl, 1 mM EDTA, 1% Triton X-100, protease (cOmplete, Roche) and phosphatase (PhosSTOP, Roche) inhibitor tablets]. After a 20 min of incubation on ice, the protein extract was separated from cell debris by centrifugation (10 min; 9,500 g, 4°C). One milligram of proteins was incubated with peptide-coupled streptavidin beads in a total volume of 1 ml of PDB3 at 4°C for 3 h, under constant agitation. The beads were washed three times with 1 ml of PDB3, and proteins were eluted with Laemmli buffer.

For pull-down assays of recombinant proteins, the affinity resin was prepared by incubating 20 nmol of biotinylated peptide with 15 µl of streptavidin beads (PureProteome Streptavidin Magnetic Beads, Merck) in 1 ml of PDB4 [50 mM Tris-HCl pH 7.4, 75 mM NaCl, 1 mM EDTA, 1% Triton X-100, 1 mM DTT, protease inhibitor tablets (cOmplete, Roche)]. The beads were washed three times with 1 ml of PDB4, and a specific binding sites were blocked with BSA (20 µg) at 4°C for 1 h, under constant agitation. The beads were then washed three times with 1 ml of PDB4. Thirty micrograms of recombinant protein with 20 µg of BSA were incubated in a total volume of 1 ml of PDB5 [50 mM Tris-HCl pH 7.4, 75 mM NaCl, 1 mM EDTA, 1% Triton X-100, 0.25 mM DTT, protease inhibitor tablets (cOmplete, Roche)] at 4°C for 2 h, under constant agitation. The beads were washed five times with 1 ml of PDB5, and proteins were eluted at room temperature with Laemmli buffer.

GFP-Trap

GFP-Trap beads (GFP-Trap_MA, Chromotek) were washed three times with 1 ml of cold PDB6 buffer [50 mM Tris-HCl pH 7.4, 50 mM NaCl, 1 mM EDTA, 1% Triton X-100, protease inhibitor tablets (cOmplete, Roche)]. GFP-VAP-A (WT or KD/MD mutant), GFP-VAP-B, or GFP-MOSPD2 stably expressing cells were transfected with plasmids expressing wild-type or mutant STARD3. Two days after transfection, adherent cells were washed two times with cold PBS and lysed in PDB6. The protein extract (500 µg of proteins) was incubated with 20 µl of beads in a total volume of 1 ml at 4°C for 2 h, under constant agitation. The beads were washed three times with 1 ml of PDB6, and proteins were eluted with Laemmli buffer at room temperature.

GST pull-down

HeLa cells were transfected with a plasmid expressing the GST-STARD3 fusion protein. Two days after transfection, adherent cells were washed 2 times with cold TBS1 (248 mM Tris-HCl pH 7.5, 137 mM NaCl, 27 mM KCl) and lysed in PDB7 [50 mM Tris-HCl pH 7.4, 150 mM NaCl, 1 mM EDTA, 1% Triton X-100, protease (cOmplete, Roche) and phosphatase (PhosSTOP, Roche) inhibitor tablets]. Glutathione Sepharose 4B beads (GE Healthcare) were washed three times with 1 ml of cold PDB7 buffer. The protein extract (1.5 mg of proteins) was incubated with 80 µl of beads in a total volume of 1 ml at 4°C for 2 h, under constant agitation. The beads were washed twice with PDB2 containing PhosSTOP, two times with PDB8 [50 mM Tris-HCl pH 7.4, 1 M NaCl, 1 mM EDTA, 1% Triton X-100, protease inhibitor tablets (cOmplete, Roche),

PhosSTOP (Roche)] and one time with PDB7. Proteins were eluted at room temperature with Laemmli buffer.

STARD3 immunoprecipitation

Fifty microliters of protein A and 50 µl of protein G sepharose (GE Healthcare) were washed three times with 1 ml of cold PDB7 buffer. HeLa or HCC1954 cells were washed two times with cold TBS1 and lysed in PDB7. The protein extract (500 µg) was incubated with 4 µg of rabbit anti-STARD3 antibody (1611) in a total volume of 1 ml at 4°C for 2 h, under constant agitation. Protein A/G sepharose was added and incubated at 4°C overnight under constant agitation. The beads were washed two times with PDB7, and proteins were eluted at room temperature with Laemmli buffer.

SDS-PAGE, Western blot, CIP treatment, and Coomassie Blue staining

SDS-PAGE and Western blot analysis were performed as previously described (Alpy *et al*, 2005). For STARD3 protein detection, the samples were not boiled. Note that an additional low molecular weight band is present for GFP-tagged proteins that are not boiled before loading. The following antibodies were used as follows: rabbit anti-GFP (1:5,000; GFP-2A3, Merck), rabbit anti-FLAG (1:1,000; F7425, Sigma), mouse anti-VAP-A (1:1,000; 4C12, Santa Cruz Biotechnology, sc-293278), rabbit anti-VAP-B [1:1,000; kind gift from Dr. L. Dupuis (Kabashi *et al*, 2013)], mouse anti-MOSPD2 [1:7; 1MOS-4E10, (Di Mattia *et al*, 2018)], mouse anti-STARD3 [1:1,000; 3G11, (Wilhelm *et al*, 2017)], rabbit anti-STARD3 pS₂₀₉ (1:1,000; 3144), mouse anti-eIF4A3 [1:1,000; 2E5, (Daguenet *et al*, 2012)], and mouse anti-actin (1:5,000; ACT-2D7, Euromedex). For phospho-specific antibodies, nitrocellulose membranes were blocked and incubated with the primary antibody in TBS2 (20 mM Tris-HCl pH 7.5, 137 mM NaCl) containing 5% BSA and 0.1% Tween 20 (TBSBT). Washes and secondary antibody incubation were performed in TBST (TBS2 buffer containing 0.1% Tween 20).

For calf intestinal alkaline phosphatase (CIP) treatment, the nitrocellulose membrane was blocked in TBS2 buffer containing 5% BSA and 0.1% Triton X-100, at room temperature for 45 min. The membrane was then incubated in CIP buffer (50 mM Tris-HCl pH 9, 1 mM MgCl₂, 0.1 mM ZnCl₂) containing 1 U/ml CIP, at 37°C for 1 h. Primary antibodies were then incubated in TBST at 4°C.

Protein gels were stained with Coomassie blue (PageBlue Protein Staining Solution, Thermo Fisher Scientific) or with fluorescent SYPRO Orange stain (Thermo Fisher Scientific).

Mass spectrometry

Samples were reduced (5 mM TCEP for 30 min at RT) and alkylated (10 mM Iodoacetamide for 30 min at RT in the dark). Two types of digestion were performed: (i) digestion with LysC (1:100) for 4 h at 37°C [in 0.1 M Tris pH 8.5, 2 mM CaCl₂] followed by trypsin (1:100) digestion overnight at 37°C. (ii) Digestion with chymotrypsin [in 0.1 M Tris pH 8.5, 10 mM CaCl₂] overnight at 25°C. Peptides were then analyzed with a nano-LC-MS/MS system (Ultimate nano-LC and LTQ Orbitrap, Thermo Fisher Scientific). Briefly, peptides were separated on a C18 nano-column with a 1–30% linear gradient of acetonitrile and analyzed with a TOP20, TOP15, and TOP10 CID or

HCD data-dependent MS method. Peptides were identified with SequestHT algorithm in Proteome Discoverer 2.2 (Thermo Fisher Scientific) using Human SwissProt database (20,368 sequences). Precursor and fragment mass tolerance were set at 7 ppm and 0.6 Da, respectively. Trypsin or chymotrypsin was set as enzyme, and up to two missed cleavages were allowed. Oxidation (M) and phosphorylation (S) were set as variable modifications, and carbamidomethylation (C) as fixed modification. Proteins were identified with a minimum of two unique peptides and were filtered with a 1% FDR (false discovery rate). Probabilities of phosphorylation for all potential phosphorylation sites were determined with PhosphoRS (Taus *et al.*, 2011).

cSTD3 recombinant protein was analyzed by liquid chromatography coupled to a mass spectrometer equipped with a heated electrospray ionization (HESI) probe. HPLC was performed using a Dionex U3000 RSCL Instrument. The injection volume was fixed at 5 μ l (Ultimate 3000, Thermo Fisher Scientific). Protein analysis was performed on a 2.1 mm i.d. \times 100 mm (3.5 μ m, 300 \AA) Xbridge Protein BEH C4 column at a flow rate of 250 μ l/min. The elution program was based on water (solvent A) and acetonitrile (solvent B) both containing 0.1% formic acid (*v/v*): 0 min 5% B, 24 min 80% B, 25 min 90% B. The Q-exactive plus spectrometer completely controlled by the Xcalibur software was operating in electrospray-positive mode. Typical ESI conditions were as follows: electrospray voltage 4 kV; capillary temperature 320°C, probe temperature 325°C, sheath gas flow 30U and auxiliary gas 10U. The MS scan was acquired in the 500–1,800 *m/z* range with the resolution set to 140,000. Data analysis was performed with BioPharma Finder, and intact protein spectra were automatically deconvoluted with ReSpect (precursor mass between 23,000 and 33,000 Da and 20 ppm mass tolerance, charge state range between 15 and 45).

Surface plasmon resonance

SPR data were collected on a Biacore T200 instrument (GE Healthcare) at 25°C with autosampler rack base cooled at 15°C. Briefly, a CM5 sensor surface was first conditioned with 10 mM HCl, 50 mM NaOH, 0.1% SDS, and 1 M NaCl pulses and extensively washed before attaching reasonable amount of streptavidin (a few hundred RU) using the standard EDC/NHS protocol provided by the manufacturer, followed by immobilization of biotinylated peptides. In order to minimize SPR artifact effects, the levels of immobilized peptides (50 RU) were kept low by injecting a highly diluted peptide solution (1–10 ng/ml) at a high flow rate (90 μ l/min). The running buffer for kinetics measurements was 50 mM Tris-HCl pH 7.0, 75 mM NaCl (filtered through a 0.22 μ m membrane), supplemented with 0.005% (*v/v*) surfactant polysorbate 20 (P20, GE Healthcare). The control peptide was immobilized on one flow cell of every chip in order to serve as a control for non-specific binding of the analyte to the matrix and for monitoring changes in solution refractive index. Analytes were simultaneously injected over the four flow cells at 8–12 different monomer concentrations ranging between 0 and 20 μ M. At least three concentrations have been duplicated in non-consecutive cycles to check for signal reproducibility. Injection and post-injection times were 120 and 180 s, respectively. The flow rate was 50 μ l/min. Data were initially processed using the BiaEvaluation 3.2 software (GE Healthcare) using “double referencing” (Fournane *et al.*, 2011) in which sensorgrams were corrected for both buffer effects and bulk

refractive index changes. The steady-state binding signal (R_{eq}) was derived by averaging the signals in a 5-s window at equilibrium in the association phase. Subsequently, steady-state analysis using in-house Python scripts was performed by fitting the average signal R_{eq} as a function of total analyte concentration, assuming a simple 1:1 interaction binding isotherm model. Note that the analyte concentration was considered according to dimers for VAP-A and VAP-B, and monomers for MOSPD2. The quality of the fit was assessed by two criteria: (i) the match of the fitted maximum capacity of the surface (R_{max}) with the expected maximum capacity (R_{theo}) inferred from the immobilized level of biotinylated peptide and (ii) the chi-square parameter which is a statistical measure of how closely the model fits the experimental data. The square root of this parameter should always be below 10% of the globally fitted R_{max} values (BiaEvaluation software user manual, 2005). The values and uncertainties of the R_{max} and K_D fitted parameters were estimated with a Monte Carlo approach by reproducing the fit using 1,000 datasets in which noise fluctuations were introduced, and then calculating the mean and the standard deviation of the obtained parameters, respectively.

Lipids

DOPC (1,2-dioleoyl-*sn*-glycero-3-phosphocholine); DNS-PE (1,2-dioleoyl-*sn*-glycero-3-phosphoethanolamine-N-(5-dimethylamino-1-naphthalenesulfonyl)); NBD-PE (1,2-dioleoyl-*sn*-glycero-3-phosphoethanolamine-N-(7-nitro-2-1,3-benzoxadiazol-4-yl)); DOGS-NTA-Ni²⁺ (1,2-dioleoyl-*sn*-glycero-3-[(N-(5-amino-1-carboxypentyl) iminodiacetic acid) succinyl]); 18:1/18:1 MPB-PE (1,2-dioleoyl-*sn*-glycero-3-phosphoethanolamine-N-[4-(*p*-maleimidophenyl) butyramide]); 18:1/18:1 NBD-PE (1,2-dioleoyl-*sn*-glycero-3-phosphoethanolamine-N-(7-nitro-2-1,3-benzoxadiazol-4-yl)); and 18:1/18:1 Liss Rhod-PE (1,2-dioleoyl-*sn*-glycero-3-phosphoethanolamine-N-(lissamine rhodamine B sulfonyl)) were purchased from Avanti Polar Lipids. Dehydroergosterol (DHE) was from Sigma-Aldrich. The concentration of DHE in stock solution in methanol was determined by UV-spectroscopy using an extinction coefficient of 13,000/M/cm.

Liposome preparation

Lipids stored in stock solutions in chloroform or methanol were mixed at the desired molar ratio. The solvent was removed in a rotary evaporator under vacuum. DOGS-NTA-Ni²⁺ and MPB-PE lipid films were pre-warmed to 33°C for 5 min prior to drying. The films were hydrated in TN2 buffer (50 mM Tris-HCl pH 7.4, 120 mM NaCl) to obtain a suspension of multilamellar liposomes. The suspension was extruded through a polycarbonate filter of 0.2 μ m pore size using a mini-extruder (Avanti Polar Lipids).

Liposome flotation assay

Each protein (cSTD3 and pS₂₀₉ cSTD3 at 1.5 μ M) was incubated with NBD-PE-containing liposomes (750 μ M total lipids) in 150 μ l of TN2 buffer at room temperature for 10 min under agitation. The suspension was adjusted to 28% (*w/w*) sucrose by mixing 100 μ l of a 60% (*w/w*) sucrose solution in TN2 buffer and overlaid with 200 μ l of TN2 buffer containing 24% (*w/w*) sucrose and 50 μ l of sucrose-free TN2 buffer. The sample was centrifuged at 240,000 $\times g$ in a swing rotor (TLS 55 Beckmann) for 1 h. The

bottom (250 μ l), middle (150 μ l), and top (100 μ l) fractions were collected. The bottom and top fractions were analyzed by SDS-PAGE using SYPRO Orange staining and a FUSION FX fluorescence imaging system.

Dynamic light scattering measurements of liposome aggregation

The experiments were performed at 25°C in a Dynapro apparatus (Protein Solutions). L_A liposomes (DOPC 97 mol% and MPB-PE 3 mol%, 50 μ M total lipids) in 20 μ l of freshly degassed TN3 buffer (50 mM Tris-HCl pH 8, 75 mM NaCl) were added to the quartz cell. A first set of about 12 autocorrelation curves was acquired to measure the size distribution of initial liposome suspension. Then, cSTD3 or pS₂₀₉ cSTD3 (380 nM final concentration) was added manually and mixed thoroughly. After a 5 min of incubation, L_B liposomes (DOPC 90 mol% and DOGS-NTA-Ni²⁺ 10 mol%, 50 μ M total lipids) were added followed by the addition of VAP-A_{His6} (700 nM). For all the experiments, the kinetics of aggregation was measured by acquiring one autocorrelation curve every 10 s. At the end of the experiment, a set of 12 autocorrelation functions was acquired. The data were analyzed using two different algorithms provided by the Dynamics v6.1 software (Protein Solutions). During the kinetics, the autocorrelation functions were fitted assuming that the size distribution is a simple Gaussian function. This mode, referred to as the monomodal or cumulant algorithm, gives a mean hydrodynamic radius, R_H , and the width (or polydispersity). The polydispersity is represented in the kinetics measurements by the shaded area and can reach very large values because of the simultaneous presence of free liposomes and of liposome aggregates of various size. Before and after the aggregation process, the autocorrelation functions were fitted using a more refined algorithm, referred as a regularization algorithm. This algorithm is able to resolve several populations of different sizes, such as free liposomes and liposome aggregates.

Fusion assay

Experiments were performed in a Shimadzu RF 5301-PC fluorimeter equipped with a cylindrical quartz cuvette. A suspension (570 μ l) of L_A liposomes (95 mol% DOPC, 1 mol% NBD-PE, 1 mol% Rhod-PE, 3 mol% MPB-PE, 62.5 μ M total lipids final concentration) was incubated with 475 nM pS₂₀₉ cSTD3 at 37°C under constant stirring in buffer. After 5 min, 30 μ l of a suspension of L_B liposomes (90 mol% DOPC, 10 mol% DOGS-NTA-Ni²⁺, 62.5 μ M total lipids final concentration), pre-incubated with VAP-A_{His6} (1 μ M final concentration), was added. Fusion was measured by recording the NBD-PE signal at 530 nm (bandwidth 5 nm) upon excitation at 450 nm (bandwidth 5 nm). The percentage of fusion is equal to $100 \times ((F - F_0)/(F_{max} - F_0))$ where F_0 is the signal measured before the addition of L_B liposomes decorated with VAP-A_{His6}, and F_{max} is the signal measured after adding Triton X-100 (1% v/v final concentration). Liposomes and proteins are injected from stock solutions with Hamilton syringes through a guide in the cover of the fluorimeter.

DHE transport assay

Experiments were carried out in a Shimadzu RF 5301-PC fluorimeter equipped with a cylindrical quartz cuvette. A suspension (570 μ l) of L_A liposomes (62.5 μ M total lipids final concentration) made of

DOPC and containing 3 mol% MPB-PE was incubated with 475 nM cSTD3 or pS₂₀₉ cSTD3 at 37°C under constant stirring in TN3 buffer. After 5 min, 30 μ l of a suspension of L_B liposomes (77.5 mol% DOPC, 10 mol% DHE, 2.5 mol% DNS-PE, 10 mol% DOGS-NTA-Ni²⁺, 62.5 μ M total lipids final concentration), pre-incubated or not with VAP-A_{His6} or VAP-A (KD/MD)_{His6} (1 μ M final concentration) was added. Lipid transport was measured by recording the DNS-PE signal at 525 nm (bandwidth 10 nm) upon DHE excitation at 310 nm (bandwidth 1.5 nm). The quantity of DHE transported from L_B to L_A membrane is expressed in mol% DHE in L_B liposomes. It is equal to $10 \times ((F - F_0)/(F_{max} - F_0))$ where F_{max} is the signal measured in the absence of pS₂₀₉ cSTD3 upon the addition of L_B liposomes and F_0 is the signal measured upon total DHE extraction by 10 mM methyl- β -cyclodextrin (Sigma). Liposomes and proteins are injected from stock solutions with Hamilton syringes through a guide in the cover of the fluorimeter.

Immunofluorescence

Cells were grown on glass coverslips, fixed in 4% paraformaldehyde in PBS, and permeabilized with 0.1% Triton X-100 in PBS. After blocking with 1% bovine serum albumin in PBS (PBS-BSA), cells were incubated overnight at 4°C with the primary antibody in PBS-BSA (rabbit anti-Flag; 1:1,000; F7425, Sigma). Cells were washed twice in PBS and incubated for 30 min with AlexaFluor 555 donkey anti-rabbit secondary antibodies (Thermo Fisher Scientific). After two washes with PBS, the slides were mounted in ProLong Gold (Invitrogen). Observations were made with a confocal microscope (Leica TCS SP5 inverted, 63 \times , NA 1.4).

For filipin staining, cells transduced with pLVX-TRE3G (encoding STARD3 wild-type and mutants) and pLVX-Tet3G vectors were treated for 48 h with 100 ng/ml doxycycline. Intracellular cholesterol labeling using filipin was performed as previously described (Wilhelm *et al*, 2017, 2019). Cells were incubated with anti-STARD3 (1611; 1:2000; IGBMC) and anti-Lamp1 (H4A3; 1:50; Developmental Studies Hybridoma Bank) antibodies. Nuclei were stained with TO-PRO-3 (1:1000; Thermo Fisher Scientific). The Fiji software was used to quantify filipin fluorescence intensity (<http://fiji.sc/>). The macro code is deposited in GitHub: https://github.com/fabienalpy/Fiji_Filipin_Staining_Quantification_Endosome_Mask. Cell contours were manually segmented, and Lamp1 signal was used to build a segmentation mask corresponding to late endosomes. The mask was then applied to the filipin image, and the mean filipin intensity in endosomes for each individual cell was measured (Appendix Fig S4).

Colocalization analysis

Colocalization was visualized using the colocalization highlighter plug-in for ImageJ. Pearson correlation coefficient was determined using the Colocalization Threshold plug-in in Fiji software. The auto-thresholding was performed using the Costes method (Costes *et al*, 2004).

Crystallization

The crystallization experiments were carried out by the sitting drop vapor diffusion method at 293 K using a Mosquito Crystal nanolitre

dispensing robot (SPT Labtech). A mixture of protein solution (in GF buffer) and reservoir solution was equilibrated against 50 μ l of reservoir solution. Several commercially available screens were used, including the JCSG + suite, the Classics suite, the PACT suite, the PEGs suite (Qiagen), Morpheus, BCS (Molecular Dimensions), Wizard Classic 1 & 2 (Rigaku), and the TOP96 (in-house) (Fazio et al, 2014).

Crystallization of VAP-A (8–212) in complex with the phosphorylated FFAT of STARD3 (GALpSEGQFYpSPPEpSFAG): The MSP domain of VAP-A (30 mg/ml) was mixed with the peptide (1:2 molar ratio); 0.2 μ l of this solution was mixed with 0.2 μ l of reservoir solution. One crystal appeared after 10 weeks in condition 18 of the PEGs suite (25% PEG 2000 MME, 0.1 M HEPES-NaOH pH 7.5), reaching full size after a further 3 weeks. The crystal was flash-frozen by direct immersion in liquid nitrogen without further cryo-protection.

Crystallization of MOSPD2 (282–490) in complex with the conventional FFAT of ORP1 (Biotin-GAMRSILSEDEFYDALSDSES): The MSP domain of MOSPD2 (25 mg/ml) was mixed with the peptide (1:1.2 molar ratio); 0.15 μ l of this solution was mixed with 0.15 μ l of reservoir solution. Plates were checked for crystal appearance over 6 months without any result. Twelve months later, a final check was made before discarding the plates, and crystals were found in 10 drops, all containing a PEG/salt mixture. The best crystal was obtained in condition 18 of the TOP96 screen (20% PEG 3350, 0.2 M Na₂SO₄). This crystal was transferred to a solution containing 25% PEG 3350, 0.2 M Na₂SO₄ and 10% glycerol, and flash-frozen in liquid nitrogen.

Crystallization of MOSPD2 (282–490) in unbound form: The MSP domain of MOSPD2 was prepared at 19 mg/ml and mixed with the Proti-Ace Kit (Hampton Research) for *in situ* proteolysis experiments. Alpha-chymotrypsin, trypsin, elastase, papain, subtilisin, and endoproteinase Glu-C were prepared as described in the protocol and mixed all together with the protein to create a proteases: sample ratio of 1:190 (*w/w*). A mix of 0.1 μ l of protein solution and 0.1 μ l of reservoir solution was used. One crystal appeared after only 12 h in condition 30 of the JCSG + suite (40% PEG 300, 0.1 M Sodium Phosphate Citrate pH 4.2), reaching full size after 8 days. The crystal was flash-frozen by direct immersion in liquid nitrogen without further cryo-protection.

Crystallization of MOSPD2 (315–445) in complex with the phosphorylated FFAT of STARD3 (CLFSGALpSEGQFYpSPPEpSFAG): The MSP domain of MOSPD2 (21 mg/ml) was mixed with the peptide (1:2 molar ratio); 0.2 μ l of this solution was mixed with 0.1 μ l of reservoir solution. Crystals appeared after 3 weeks in condition 53 of the BCS screen (7.5% PEG 2000, 7.5% PEG 3350, 7.5% PEG 4000, 7.5% PEG 5000 MME, 0.05 M MgSO₄, 0.1 M HEPES-NaOH pH 7.5), reaching full size after a further 2 weeks. Crystals were transferred to the same solution supplemented with 15% glycerol, and flash cooled in liquid nitrogen.

Data collection and structure determination

All data were collected from crystals at 100 K, as detailed below, and processed, integrated, and scaled using XDS (Kabsch, 2010). All molecular replacement was performed using PHASER (McCoy et al, 2007) in the PHENIX suite (Liebschner et al, 2019). Refinement of the structures was performed using PHENIX and BUSTER (Smart

et al, 2012; Bricogne et al, 2019) with iterative model building performed in COOT (Emsley et al, 2010). The quality of the final refined models was assessed using MOLPROBITY (Williams et al, 2018) and PROCHECK (Laskowski et al, 1993). Data collection and refinement statistics are given in Table EV3. Structural figures were prepared using PyMOL (www.pymol.org). Surface coloring was performed with the YRB scheme with all carbon atoms not bound to nitrogen and oxygen atoms in yellow, nitrogen atoms of K and R in blue, oxygen of D and E in red, and all the remaining atoms in white (Hagemans et al, 2015).

For the complex of VAP-A (8–212: MSP and coiled-coil domains) with the phosphorylated FFAT motif of STARD3 (200–216), data were collected from two fragments of the same crystal on a PILATUS 6M detector (Dectris) at the ID23-1 beamline of the ESRF and using the MxCuBE software (Gabadinho et al, 2010). After data processing, the two datasets were scaled together using XSCALE, and anisotropic truncation and correction were performed on the merged dataset using the STARANISO server (Tickle et al, 2018). The crystal diffracted anisotropically to 1.85 Å (3.0 Å in the worst direction) and belonged to the primitive triclinic space group P1, with unit cell dimensions $a = 39.1$ Å, $b = 43.8$ Å, $c = 83.7$ Å, $\alpha = 89.46^\circ$, $\beta = 92.91^\circ$, $\gamma = 105.13^\circ$. The structure was solved by molecular replacement using a monomer of the MSP domain of rat VAP-A (Kaiser et al, 2005) (PDB ID: 1Z90) as a search model. The asymmetric unit contains four copies of the MSP domain (~residues 9–135) and two copies of the peptide, with a corresponding Matthews' coefficient (Matthews, 1968) of 2.21 Å³/Da and a solvent content of approximately 44%. The asymmetric unit is too small to contain four copies of the construct crystallized, indicating that the coiled-coil domain was cleaved in the drop, and is not present as a disordered domain in the crystal.

For the complex of MOSPD2 (282–490) with the conventional FFAT of ORP1 (469–485), data were collected on an EIGER X 9M detector (Dectris) at the Proxima 2A beamline of Synchrotron SOLEIL. The crystal diffracted to 2.3 Å and belonged to a primitive hexagonal space group (P6₁22 or P6₅22) with unit cell dimensions $a = b = 126.9$ Å, $c = 184.4$ Å. The first model from the NMR structure of the MSP domain of MOSPD2 (PDB ID: 1WIC) was extracted and truncated to the rigid core, and used as a search model in PHASER with a solution found in P6₁22. The asymmetric unit contains six copies of the MSP domain (~residues 315–447) and five copies of the peptide, with a corresponding Matthews' coefficient of 2.16 Å³/Da and a solvent content of approximately 43%. As with VAP-A, the asymmetric unit is too small to contain six copies of the construct crystallized, implying that the N- and C-terminal extensions had been cleaved in the drop during the long crystallization time.

For unbound MOSPD2 [282-490], data were collected on our in-house diffractometer. The diffractometer comprises an FR-X rotating anode X-ray generator (Rigaku) fitted with Osmic VariMax HF Arc) Sec confocal optics and an EIGER R 4M detector (Dectris). The crystal diffracted to 1.5 Å and belonged to the primitive orthorhombic space group P2₁2₁2₁ with unit cell dimensions $a = 28.1$ Å, $b = 51.2$ Å, $c = 78.8$ Å. The structure was solved by molecular replacement using a monomer of our MOSPD2/ORP1 complex structure. The asymmetric unit contains one copy of the MSP domain (residues 315–445) with a corresponding Matthews' coefficient of 1.97 Å³/Da and a solvent content of approximately 38%.

For the complex of MOSPD2 (315–445) with the phosphorylated FFAT motif of STARD3 (196–216), data were collected on an EIGER X 9M detector (Dectris) at the Proxima 2A beamline of Synchrotron SOLEIL. The crystal diffracted to 2.35 Å and belonged to a primitive tetragonal space group (P4₁2₁2 or P4₃2₁2) with unit cell dimensions $a = b = 87.9$ Å, $c = 95.1$ Å. The structure was solved by molecular replacement in PHASER using our MOSPD2 MSP domain unbound structure as a search model with a solution found in P4₁2₁2. The asymmetric unit contains two copies of the MOSPD2 MSP domain/STARD3 FFAT motif complex with a corresponding Matthews' coefficient of 1.97 Å³/Da and a solvent content of approximately 38%.

In silico identification of Phospho-FFATs

The algorithm used for Phospho-FFAT identification is derived from the position weight matrix shown in Table EV4. The scoring system is based on 19 continuous residues: the seven residues forming the core, six residues upstream, and it is extended from the matrix previously described to include the six residues downstream (Slee & Levine, 2019). These residues were allocated a score in the position weight matrix. All residues in all human protein sequences obtained from UniProt were scored by scripts enacted in Python. Thus, for proteins with n residues, n scores were calculated; the two best scores (named SCORE1 and SCORE2) are shown Tables EV1 and EV2. Venn diagrams and sequence logos were constructed using InteractiVenn and Weblogo, respectively (Crooks *et al.*, 2004; Heberle *et al.*, 2015).

Statistical analyses

Statistical analyses were performed using the Mann–Whitney, or the Kruskal–Wallis non-parametric tests (Prism, GraphPad). In the latter case, all conditions were compared with the Dunn's multiple comparison test. P -values < 0.05 , < 0.01 , and < 0.001 are identified with 1, 2, and 3 asterisks, respectively. ns: $P \geq 0.05$. The number of replicates (n) used for calculating statistics is specified in the figure legends. For Pearson correlation coefficient calculations, individual cells from at least three independent experiments were used for calculating statistics.

Data availability

The coordinates and structure factors have been deposited in the Protein Data Bank under the accession codes 6TQR (<http://www.rcsb.org/pdb/explore/explore.do?structureId=6TQR>; VAP-A/STARD3 complex), 6TQS (<http://www.rcsb.org/pdb/explore/explore.do?structureId=6TQS>; MOSPD2/ORP1 complex), 6TQT (<http://www.rcsb.org/pdb/explore/explore.do?structureId=6TQT>; MOSPD2 unbound), and 6TQU (<http://www.rcsb.org/pdb/explore/explore.do?structureId=6TQU>; MOSPD2/STARD3 complex).

Expanded View for this article is available online.

Acknowledgements

We thank the members of the Molecular and Cellular Biology of Breast Cancer team (IGBMC) for helpful advice and discussions. We thank Julie Milanini (IPMC) and the IGBMC cell culture facility (Betty Heller), imaging

center (Bertrand Vernay, Elvire Guiot, and Erwan Grandgirard), polyclonal and monoclonal antibody facility (Gilles Duval and Mustapha Oulad-Abdelghani), proteomics platform (Luc Negroni and Bastien Morlet), and structural biology and genomics platform (Catherine Birck) for their excellent technical assistance. We thank Delphine Debayle for helping us to determine the molecular weight of cSTD3 constructs by mass spectrometry. We wish to thank Luc Dupuis (INSERM U118, Strasbourg, FR) for providing the anti-VAP-B antibody. We acknowledge the European Synchrotron Radiation Facility (proposal number MX-1636) and SOLEIL (proposal number 20170871) for provision of synchrotron radiation facilities, and we would like to thank Andrew McCarthy for assistance in using beamline ID23-1, and William Shepard and Martin Savko for assistance in using beamline Proxima 2A. T.D.M. received a fellowship from the Fondation pour la Recherche Médicale (<https://www.frm.org/>). A.M. and L.V. received an allocation from the Ministère de l'Enseignement Supérieur et de la Recherche (France; <http://www.enseignementsup-recherche.gouv.fr/>). This work was supported by grants from the Agence Nationale de la Recherche ANR (grant ANR-19-CE44-0003; <https://anr.fr/>), and from the Ligue Contre le Cancer (Conférence de Coordination Interrégionale du Grand Est; <https://www.ligue-cancer.net>), SEVE Sein et Vie, the Institut National Du Cancer INCA (INCA_9269; www.e-cancer.fr), by the French Infrastructure for Integrated Structural Biology (FRISBI) ANR-10-INSB-05-01 and INSTRUCT-ERIC. We also acknowledge funds from the Institut National de Santé et de Recherche Médicale (<http://www.inserm.fr/>), the Centre National de la Recherche Scientifique (<http://www.cnrs.fr/>), the Université de Strasbourg (<http://www.unistra.fr>), and the grant ANR-10-LABX-0030-INRT, a French State fund managed by the Agence Nationale de la Recherche under the frame program Investissements d'Avenir ANR-10-IDEX-0002-02.

Author contributions

FA, CT, and GD conceived and supervised the project. TDM and AM performed and analyzed most of the biochemistry and cell biology experiments, with the help of CW, CT, and FA. SI and GD performed and analyzed all *in vitro* membrane tethering/sterol transport experiments. LV performed *in vivo* cholesterol labeling experiments with the help of TDM and AM. YN conceived, performed, and analyzed the SPR experiments. PE synthesized the peptides. FR performed and analyzed mass spectrometry experiments. JS and TPL conceived and coded the algorithm identifying Phospho-FFATs, with the help of AM and FA. PP-C crystallized the different complexes. AGM collected the X-ray diffraction data and solved the structures, with the help of JC. FA, CT, GD, AGM, and YN wrote the manuscript and prepared the figures, with the help of TDM and AM. All authors commented on the manuscript.

Conflict of interest

The authors declare that they have no conflict of interest.

References

- Alli-Balogun GO, Levine TP (2019) Regulation of targeting determinants in interorganelle communication. *Curr Opin Cell Biol* 57: 106–114
- Alpy F, Wendling C, Rio M-C, Tomasetto C (2002) MENTHO, a MLN64 homologue devoid of the START domain. *J Biol Chem* 277: 50780–50787
- Alpy F, Latchumanan VK, Kedinger V, Janoshazi A, Thiele C, Wendling C, Rio M-C, Tomasetto C (2005) Functional characterization of the MENTAL domain. *J Biol Chem* 280: 17945–17952

- Alpy F, Tomasetto C (2005) Give lipids a START: the StAR-related lipid transfer (START) domain in mammals. *J Cell Sci* 118: 2791–2801
- Alpy F, Rousseau A, Schwab Y, Legueux F, Stoll I, Wendling C, Spiegelhalter C, Kessler P, Mathelin C, Rio M-C et al (2013) STARD3 or STARD3NL and VAP form a novel molecular tether between late endosomes and the ER. *J Cell Sci* 126: 5500–5512
- Amarilio R, Ramachandran S, Sabanay H, Lev S (2005) Differential regulation of endoplasmic reticulum structure through VAP-Nir protein interaction. *J Biol Chem* 280: 5934–5944
- Balla T, Kim YJ, Alvarez-Prats A, Pemberton J (2019) Lipid dynamics at contact sites between the endoplasmic reticulum and other organelles. *Annu Rev Cell Dev Biol* 35: 85–109
- Bonifacino JS, Rojas R (2006) Retrograde transport from endosomes to the trans-Golgi network. *Nat Rev Mol Cell Biol* 7: 568–579
- Bricogne G, Blanc E, Brandl M, Flensburg C, Keller P, Paciorek W, Roversi P, Sharff A, Smart O, Vonrhein C et al (2019) *BUSTER version 2.10.2*, Cambridge, UK: Global Phasing Ltd
- Costello JL, Castro IG, Hacker C, Schrader TA, Metz J, Zeuschner D, Azadi AS, Godinho LF, Costina V, Findeisen P et al (2017a) ACBD5 and VAPB mediate membrane associations between peroxisomes and the ER. *J Cell Biol* 216: 331–342
- Costello JL, Castro IG, Schrader TA, Islinger M, Schrader M (2017b) Peroxisomal ACBD4 interacts with VAPB and promotes ER-peroxisome associations. *Cell Cycle* 16: 1039–1045
- Costes SV, Daelemans D, Cho EH, Dobbin Z, Pavlakis G, Lockett S (2004) Automatic and quantitative measurement of protein-protein colocalization in live cells. *Biophys J* 86: 3993–4003
- Crooks GE, Hon G, Chandonia J-M, Brenner SE (2004) WebLogo: a sequence logo generator. *Genome Res* 14: 1188–1190
- Dagueuet E, Bagueuet A, Degot S, Schmidt U, Alpy F, Wendling C, Spiegelhalter C, Kessler P, Rio M-C, Le Hir H et al (2012) Perispeckles are major assembly sites for the exon junction core complex. *Mol Biol Cell* 23: 1765–1782
- De Vos KJ, Morotz GM, Stoica R, Tudor EL, Lau KF, Ackerley S, Warley A, Shaw CE, Miller CC (2012) VAPB interacts with the mitochondrial protein PTP1B1 to regulate calcium homeostasis. *Hum Mol Genet* 21: 1299–1311
- Di Mattia T, Wilhelm LP, Ikhlef S, Wendling C, Spehner D, Nominé Y, Giordano F, Mathelin C, Drin G, Tomasetto C et al (2018) Identification of MOSPD2, a novel scaffold for endoplasmic reticulum membrane contact sites. *EMBO Rep* 19: e45453
- Dong R, Saheki Y, Swarup S, Lucast L, Harper JW, De Camilli P (2016) Endosome-ER contacts control actin nucleation and retromer function through VAP-dependent regulation of PI4P. *Cell* 166: 408–423
- Emsley P, Lohkamp B, Scott WG, Cowtan K (2010) Features and development of Coot. *Acta Crystallogr D Biol Crystallogr* 66: 486–501
- Fazio VJ, Peat TS, Newman J (2014) A drunken search in crystallization space. *Acta Crystallogr Sect F Struct Biol Commun* 70: 1303–1311
- Fournane S, Charbonnier S, Chapelle A, Kieffer B, Orfanoudakis G, Travé G, Masson M, Nominé Y (2011) Surface plasmon resonance analysis of the binding of high-risk mucosal HPV E6 oncoproteins to the PDZ1 domain of the tight junction protein MAGI-1. *J Mol Recognit* 24: 511–523
- Fox PD, Haberkorn CJ, Akin EJ, Seel PJ, Krapf D, Tamkun MM (2015) Induction of stable ER-plasma-membrane junctions by Kv2.1 potassium channels. *J Cell Sci* 128: 2096–2105
- Freyre CAC, Rauher PC, Ejsing CS, Klemm RW. (2019) MIGA2 links mitochondria, the ER, and lipid droplets and promotes de novo lipogenesis in adipocytes. *Mol Cell* 76: 811–825.e14
- Friedman JR, Lackner LL, West M, DiBenedetto JR, Nunnari J, Voeltz GK (2011) ER tubules mark sites of mitochondrial division. *Science* 334: 358–362
- Friedman JR, DiBenedetto JR, West M, Rowland AA, Voeltz GK (2013) Endoplasmic reticulum-endosome contact increases as endosomes traffic and mature. *Mol Biol Cell* 24: 1030–1040
- Furuita K, Jee J, Fukada H, Mishima M, Kojima C (2010) Electrostatic interaction between oxysterol-binding protein and VAMP-associated protein A revealed by NMR and mutagenesis studies. *J Biol Chem* 285: 12961–12970
- Gabardinjo J, Beteva A, Guizarro M, Rey-Bakaikoa V, Spruce D, Bowler MW, Brockhauser S, Flot D, Gordon EJ, Hall DR et al (2010) MxCuBE: a synchrotron beamline control environment customized for macromolecular crystallography experiments. *J Synchrotron Radiat* 17: 700–707
- Go CD, Knight JDR, Rajasekharan A, Rathod B, Hesketh GG, Abe KT, Youn J-Y, Samavarchi-Tehrani P, Zhang H, Zhu LY et al (2019) A proximity biotinylation map of a human cell. *bioRxiv*: 796391. <https://doi.org/10.1101/796391>
- Hagemans D, van Belzen IAEM, Morán Luengo T, Rüdiger SGD (2015) A script to highlight hydrophobicity and charge on protein surfaces. *Front Mol Biosci* 2: 56
- Hara T, Takamura A, Kishi C, Iemura S, Natsume T, Guan J-L, Mizushima N (2008) FIP200, a ULK-interacting protein, is required for autophagosome formation in mammalian cells. *J Cell Biol* 181: 497–510
- Heberle H, Meirelles GV, da Silva FR, Telles GP, Minghim R (2015) InteractiVenn: a web-based tool for the analysis of sets through Venn diagrams. *BMC Bioinformatics* 16: 169
- Hönscher C, Mari M, Auffarth K, Bohnert M, Griffith J, Geerts W, van der Laan M, Cabrera M, Reggiori F, Ungermann C (2014) Cellular metabolism regulates contact sites between vacuoles and mitochondria. *Dev Cell* 30: 86–94
- Hornbeck PV, Zhang B, Murray B, Kornhauser JM, Latham V, Skrzypek E (2015) PhosphoSitePlus, 2014: mutations, PTMs and recalibrations. *Nucleic Acids Res* 43: D512–D520
- Huttlin EL, Ting L, Bruckner RJ, Gebreab F, Gygi MP, Szpyt J, Tam S, Zarraga G, Colby G, Baltier K et al (2015) The BioPlex network: a systematic exploration of the human interactome. *Cell* 162: 425–440
- Huttlin EL, Bruckner RJ, Paulo JA, Cannon JR, Ting L, Baltier K, Colby G, Gebreab F, Gygi MP, Parzen H et al (2017) Architecture of the human interactome defines protein communities and disease networks. *Nature* 545: 505–509
- Johnson B, Leek AN, Solé L, Maverick EE, Levine TP, Tamkun MM (2018) Kv2 potassium channels form endoplasmic reticulum/plasma membrane junctions via interaction with VAPA and VAPB. *Proc Natl Acad Sci USA* 115: E7331–E7340
- Kabsch W (2010) XDS. *Acta Crystallogr D Biol Crystallogr* 66: 125–132
- Kabashi E, El Oussini H, Bercier V, Gros-Louis F, Valdmanis PN, McDearmid J, Meijer IA, Dion PA, Dupre N, Hollinger D et al (2013) Investigating the contribution of VAPB/ALS8 loss of function in amyotrophic lateral sclerosis. *Hum Mol Genet* 22: 2350–2360
- Kaiser SE, Brickner JH, Reilein AR, Fenn TD, Walter P, Brunger AT (2005) Structural basis of FFAT motif-mediated ER targeting. *Structure* 13: 1035–1045
- Karplus PA, Diederichs K (2015) Assessing and maximizing data quality in macromolecular crystallography. *Curr Opin Struct Biol* 34: 60–68
- Kawano M, Kumagai K, Nishijima M, Hanada K (2006) Efficient trafficking of ceramide from the endoplasmic reticulum to the Golgi apparatus requires a VAMP-associated protein-interacting FFAT motif of CERT. *J Biol Chem* 281: 30279–30288

- Kirmiz M, Vierra NC, Palacio S, Trimmer JS (2018) Identification of VAPA and VAPB as Kv2 channel-interacting proteins defining endoplasmic reticulum-plasma membrane junctions in mammalian brain neurons. *J Neurosci* 38: 7562–7584
- Kumagai K, Kawano M, Shinkai-Ouchi F, Nishijima M, Hanada K (2007) Interorganelle trafficking of ceramide is regulated by phosphorylation-dependent cooperativity between the PH and START domains of CERT. *J Biol Chem* 282: 17758–17766
- Kumagai K, Kawano-Kawada M, Hanada K (2014) Phosphoregulation of the ceramide transport protein CERT at serine 315 in the interaction with VAMP-associated protein (VAP) for inter-organelle trafficking of ceramide in mammalian cells. *J Biol Chem* 289: 10748–10760
- Lajoie MJ, Rovner AJ, Goodman DB, Aerni H-R, Haimovich AD, Kuznetsov G, Mercer JA, Wang HH, Carr PA, Mosberg JA et al (2013) Genomically recoded organisms expand biological functions. *Science* 342: 357–360
- Larkin MA, Blackshields G, Brown NP, Chenna R, McGettigan PA, McWilliam H, Valentin F, Wallace IM, Wilm A, Lopez R et al (2007) Clustal W and Clustal X version 2.0. *Bioinformatics* 23: 2947–2948
- Laskowski RA, Moss DS, Thornton JM (1993) Main-chain bond lengths and bond angles in protein structures. *J Mol Biol* 231: 1049–1067
- Levine T, Loewen C (2006) Inter-organelle membrane contact sites: through a glass, darkly. *Curr Opin Cell Biol* 18: 371–378
- Liebschner D, Afonine PV, Baker ML, Bunkóczy G, Chen VB, Croll TI, Hintze B, Hung L-W, Jain S, McCoy AJ et al (2019) Macromolecular structure determination using X-rays, neutrons and electrons: recent developments in Phenix. *Acta Crystallogr Sect Struct Biol* 75: 861–877
- Lim ST, Antonucci DE, Scannevin RH, Trimmer JS (2000) A novel targeting signal for proximal clustering of the Kv2.1 K⁺ channel in hippocampal neurons. *Neuron* 25: 385–397
- Loewen CJR, Roy A, Levine TP (2003) A conserved ER targeting motif in three families of lipid binding proteins and in Opi1p binds VAP. *EMBO J* 22: 2025–2035
- Lord SJ, Velle KB, Mullins RD, Fritz-Laylin LK. (2020) SuperPlots: communicating reproducibility and variability in cell biology. *J Cell Biol* 219: e202001064
- Lv BF, Yu CF, Chen YY, Lu Y, Guo JH, Song QS, Ma DL, Shi TP, Wang L (2006) Protein tyrosine phosphatase interacting protein 51 (PTPIP51) is a novel mitochondria protein with an N-terminal mitochondrial targeting sequence and induces apoptosis. *Apoptosis* 11: 1489–1501
- Matthews BW (1968) Solvent content of protein crystals. *J Mol Biol* 33: 491–497
- McCoy AJ, Grosse-Kunstleve RW, Adams PD, Winn MD, Storoni LC, Read RJ (2007) Phaser crystallographic software. *J Appl Crystallogr* 40: 658–674
- McCune BT, Tang W, Lu J, Eaglesham JB, Thorne L, Mayer AE, Condiff E, Nice TJ, Goodfellow I, Krezel AM et al (2017) Noroviruses co-opt the function of host proteins VAPA and VAPB for replication via a phenylalanine–phenylalanine-acidic-tract-motif mimic in nonstructural viral protein NS1/2. *MBio* 8: e00668-17
- Mesmin B, Bigay J, Moser von Filseck J, Lacas-Gervais S, Drin G, Antony B (2013) A four-step cycle driven by PI(4)P hydrolysis directs sterol/PI(4)P exchange by the ER-Golgi tether OSBP. *Cell* 155: 830–843
- Mesmin B, Bigay J, Polidori J, Jamecna D, Lacas-Gervais S, Antony B (2017) Sterol transfer, PI4P consumption, and control of membrane lipid order by endogenous OSBP. *EMBO J* 36: 3156–3174
- Mikitova V, Levine TP (2012) Analysis of the key elements of FFAT-like motifs identifies new proteins that potentially bind VAP on the ER, including two AKAPs and FAPP2. *PLoS One* 7: e30455
- Murphy SE, Levine TP (2016) VAP, a versatile access point for the endoplasmic reticulum: review and analysis of FFAT-like motifs in the VAPome. *Biochim Biophys Acta* 1861: 952–961
- Okegawa Y, Motohashi K (2015) A simple and ultra-low cost homemade seamless ligation cloning extract (SLiCE) as an alternative to a commercially available seamless DNA cloning kit. *Biochem Biophys Rep* 4: 148–151
- Orchard S, Ammari M, Aranda B, Breuza L, Briganti L, Broackes-Carter F, Campbell NH, Chavali G, Chen C, del-Toro N et al (2014) The MintAct project—IntAct as a common curation platform for 11 molecular interaction databases. *Nucleic Acids Res* 42: D358–D363
- Oughtred R, Stark C, Breitkreutz B-J, Rust J, Boucher L, Chang C, Kolas N, O'Donnell L, Leung G, McAdam R et al (2019) The BioGRID interaction database: 2019 update. *Nucleic Acids Res* 47: D529–D541
- Park H-S, Hohn MJ, Umehara T, Guo L-T, Osborne EM, Benner J, Noren CJ, Rinehart J, Söll D (2011) Expanding the genetic code of *Escherichia coli* with phosphoserine. *Science* 333: 1151–1154
- Pirman NL, Barber KW, Aerni HR, Ma NJ, Haimovich AD, Rogulina S, Isaacs FJ, Rinehart J (2015) A flexible codon in genomically recoded *Escherichia coli* permits programmable protein phosphorylation. *Nat Commun* 6: 8130
- Prinz WA, Toulmay A, Balla T (2019) The functional universe of membrane contact sites. *Nat Rev Mol Cell Biol* 21, 7–24
- Rocha N, Kuijl C, van der Kant R, Janssen L, Houben D, Janssen H, Zwart W, Neeffes J (2009) Cholesterol sensor ORP1L contacts the ER protein VAP to control Rab7–RILP–p150Glued and late endosome positioning. *J Cell Biol* 185: 1209–1225
- Slee JA, Levine TP (2019) Systematic prediction of FFAT motifs across eukaryote proteomes identifies nucleolar and eisosome proteins with the predicted capacity to form bridges to the endoplasmic reticulum. *Contact* 2: 2515256419883136
- Smart OS, Womack TO, Flensburg C, Keller P, Paciorek W, Sharff A, Vornrhein C, Bricogne G (2012) Exploiting structure similarity in refinement: automated NCS and target-structure restraints in BUSTER. *Acta Crystallogr D Biol Crystallogr* 68: 368–380
- Stanhope R, Flora E, Bayne C, Derré I (2017) IncV, a FFAT motif-containing *Chlamydia* protein, tethers the endoplasmic reticulum to the pathogen-containing vacuole. *Proc Natl Acad Sci USA* 114: 12039–12044
- Stoica R, Vos KJD, Paillusson S, Mueller S, Sancho RM, Lau K-F, Vizcay-Barrena G, Lin W-L, Xu Y-F, Lewis J et al (2014) ER–mitochondria associations are regulated by the VAPB–PTPIP51 interaction and are disrupted by ALS/FTD-associated TDP-43. *Nat Commun* 5: ncomms4996
- Struck DK, Hoekstra D, Pagano RE (1981) Use of resonance energy transfer to monitor membrane fusion. *Biochemistry* 20: 4093–4099
- Sugiki T, Egawa D, Kumagai K, Kojima C, Fujiwara T, Takeuchi K, Shimada I, Hanada K, Takahashi H (2018) Phosphoinositide binding by the PH domain in ceramide transfer protein (CERT) is inhibited by hyperphosphorylation of an adjacent serine-repeat motif. *J Biol Chem* 293: 11206–11217
- Taus T, Köcher T, Pichler P, Paschke C, Schmidt A, Henrich C, Mechtler K (2011) Universal and confident phosphorylation site localization using phosphoRS. *J Proteome Res* 10: 5354–5362
- Tickle I, Flensburg C, Keller P, Paciorek W, Sharff A, Vornrhein C, Bricogne G (2018) STARANISO. Cambridge, UK: Global Phasing Ltd. <http://staraniso.globalphasing.org/cgi-bin/staraniso.cgi>
- Valm AM, Cohen S, Legant WR, Melunis J, Hershberg U, Wait E, Cohen AR, Davidson MW, Betzig E, Lippincott-Schwartz J (2017) Applying systems-level spectral imaging and analysis to reveal the organelle interactome. *Nature* 546: 162–167

- Waterhouse AM, Procter JB, Martin DMA, Clamp M, Barton GJ (2009) Jalview Version 2—a multiple sequence alignment editor and analysis workbench. *Bioinformatics* 25: 1189–1191
- Westrate LM, Lee JE, Prinz WA, Voeltz GK (2015) Form follows function: the importance of endoplasmic reticulum shape. *Annu Rev Biochem* 84: 791–811
- Wilhelm LP, Wendling C, Védie B, Kobayashi T, Chenard M-P, Tomasetto C, Drin G, Alpy F (2017) STARD3 mediates endoplasmic reticulum-to-endosome cholesterol transport at membrane contact sites. *EMBO J* 36: 1412–1433
- Wilhelm LP, Voilquin L, Kobayashi T, Tomasetto C, Alpy F. (2019) Intracellular and plasma membrane cholesterol labeling and quantification using filipin and GFP-D4. In *Intracellular lipid transport: methods and protocols*, Drin G (ed.) pp 137–152. New York, NY: Springer
- Williams CJ, Headd JJ, Moriarty NW, Prisant MG, Videau LL, Deis LN, Verma V, Keedy DA, Hintze BJ, Chen VB et al (2018) MolProbity: more and better reference data for improved all-atom structure validation. *Protein Sci* 27: 293–315
- Wu H, Carvalho P, Voeltz GK (2018) Here, there, and everywhere: the importance of ER membrane contact sites. *Science* 361: eaan5835
- Zhang Y, Liu X, Bai J, Tian X, Zhao X, Liu W, Duan X, Shang W, Fan H-Y, Tong C (2016) Mitoguardin regulates mitochondrial fusion through MitoPLD and is required for neuronal homeostasis. *Mol. Cell* 61: 111–124
- Zhao YG, Liu N, Miao G, Chen Y, Zhao H, Zhang H (2018) The ER contact proteins VAPA/B interact with multiple autophagy proteins to modulate autophagosome biogenesis. *Curr Biol* 28: 1234–1245.e4



License: This is an open access article under the terms of the Creative Commons Attribution-NonCommercial-NoDerivs License, which permits use and distribution in any medium, provided the original work is properly cited, the use is non-commercial and no modifications or adaptations are made.